ACS Partner Journal

CHEMICAL & BIOMEDICAL IMAGING

pubs.acs.org/ChemBioImaging

Article

An Activity-Based Sensing Approach to Monitor Nanomaterial-Promoted Changes in Labile Metal Pools in Living Systems

Javier Bonet-Aleta,* Aidan T. Pezacki, Miku Oi, Jose L. Hueso, Jesus Santamaria, and Christopher J. Chang*

Cite This: https://doi.org/10.1021/cbmi.5c00237

Read Online

ACCESS | Metrics & More | Article Recommendations | Supporting Information

ABSTRACT: Metal-based nanoparticles are a promising class of materials for diagnosis and treatment of cancer and other diseases. However, mechanisms of action of these nanomedicines remain insufficiently understood due in large part to our limited understanding of the dynamic equilibria between solid metal nanoparticles and labile metal ions generated from these nanoparticles within complex biological milieus. Here, we apply activity-based sensing to directly identify and investigate the fate of labile copper pools with metal and oxidation state-specificity generated by anticancer copper nanomedicines. We found that treatment of cells with copper-releasing nanoparticles alter labile Cu(I)/Cu(II) ratios through an increase in labile Cu(II), while overall labile copper levels decrease. Labile copper release triggers compensatory responses in two major antioxidant pathways, glutathione (GSH) and nuclear factor erythroid 2-related factor 2 (NRF2), as well as in metal homeostasis to limit copper availability via regulation of copper export (ATP7B) and copper import (CTR1) proteins. These findings establish the value of activity-based sensing as a generalizable approach for labile metal imaging to help decipher molecular mechanisms of bioactive metal nanoparticles and guide the development of more effective nanomedicine diagnostics and therapies to target metal-dependent disease vulnerabilities.

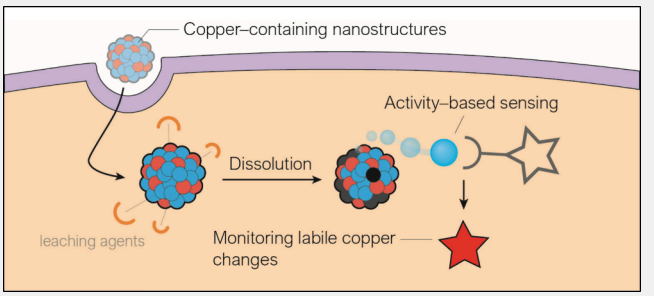

KEYWORDS: *copper nanoparticles, anticancer nanomedicines, activity-based sensing, transition metal signaling, oxidative stress*

INTRODUCTION

Nanoparticle materials offer a wealth of new opportunities in diagnosis and treatment of disease. In this context, catalytic metal-based nanoparticles show promise in cancer nanomedicine owing to their capacity to leverage unique chemical conditions within the tumor microenvironment (TME) to perform localized therapy without the need for external stimuli such as light, X-rays, or ultrasound.[1] In particular, nanoparticles are delivered with the aim of catalyzing cytotoxic chemical reactions using differential features of the TME.[2] These reaction pathways include an increased production of reactive oxygen species (ROS) in response to the higher metabolic needs associated with tumorigenesis and metastasis, along with overexpression of antioxidant-associated elements as a compensatory mechanism to maintain a suitable intracellular redox balance.[3−6] Glutathione (GSH) is of particular interest as an antioxidant whose biosynthesis and reduction have been shown to be upregulated upon oncogenic mutations.[7] Nanoparticles composed of biologically relevant metal nutrients, including copper,[8−10] iron,[11,12] manganese,[13,14] or molybdenum,[15−17] as well as noble-metals[18] or hybrids,[19] have been successfully employed to exploit the TME through their ability to simultaneously produce ROS and oxidize GSH to its disulfide form (GSSG). Studies on intracellular metal nanoparticle trafficking, including internalization/excretion mechanisms and effects on internal organelles, are prevalent in the literature.[20−23] In contrast, the fate of leached labile metal ion species derived from these nanoparticles and the corresponding cellular responses have received much less attention. Indeed, since metal ion nutrients are under strict regulation by cells, a better fundamental understanding of how metal nanoparticle treatments can influence metal homeostatic equilibria can create new therapeutic and diagnostic opportunities for nanomedicine.

Against this backdrop, copper (Cu) has emerged as a key component in a multitude of nanomedicines.[1,8,9,24−27] This metal has potent intrinsic catalytic activity that can be exploited for diagnostic and/or therapeutic purposes. On the other hand, it is also an essential nutrient for life,[28] acting as a static metabolic cofactor to regulate the enzymatic activity at protein active sites[29−33] or as a transition metal signaling agent

Received: November 19, 2025
Revised: January 4, 2026
Accepted: January 5, 2026

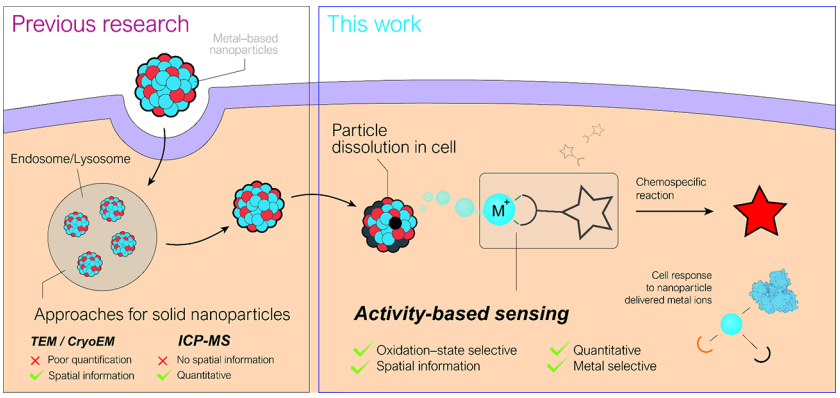

Figure 1. Copper leaches from catalytic anticancer nanoparticle therapeutics and activates cellular pathways designed to control the concentrations and bioavailability of labile copper ions, providing a distinct route from the traditional mode of action followed by solid metal nanoparticles. Activity-based sensing probes for direct labile metal imaging with element and oxidation state specificity, when used in conjunction with inhibitors or promoters of specific biochemical pathways, can reveal fundamental cellular responses to treatment with copper-based nanomedicines and mechanisms of action.

in labile forms that are loosely bound to small-molecule and protein ligands with freedom to move and exchange along different cellular locations and regulate protein function beyond active sites by metalloallostery.[34−38] Labile copper acts as a signaling agent in regulating a diverse array of biological processes, including neuronal activity and neuroinflammation,[39−42] lipid metabolism and lipolysis,[43] and kinase signaling.[44−48] However, dysregulation of biological copper homeostasis with aberrant elevations in this metal nutrient can lead to the production of harmful ROS through the Fenton reaction,[49] in addition to triggering a newly identified form of copper-dependent cell death, termed cuproptosis,[50] and thus it is strictly regulated by the cell.[51,52] Moreover, copper deficiency is as harmful as copper excess, this metal nutrient plays a key role in cell health and survival pathways, through a novel copper-dependent form of cell proliferation termed cuproplasia.[53] Thus, both the selective supplementation or sequestration of this metal nutrient in the TME could form the basis for development of novel nanomedicines.

Recent reports show how nanostructured catalysts containing copper are susceptible to copper dissolution in vitro, particularly in the presence of GSH.[54−56] Despite these observations, to the best of our knowledge the application of direct labile metal imaging to uncover regulatory mechanisms that govern the adaptation of cells to this sudden influx of metal remain limited. In this context, our laboratory has advanced the concept of activity-based sensing, which employs chemical reactivity between probe and analyte rather than molecular recognition to achieve high selectivity for molecular imaging in biological systems.[57−59] We posited that activity-based sensing could be applied to study labile copper released upon internalization and metal leaching of copper-based nanoparticles and subsequent cellular responses (Figure 1). In particular, we sought to apply a tandem activity-based sensing and labeling strategy recently developed by our laboratory which covalently anchors copper-selective fluorescent probes upon analyte detection to preserve spatial information on localized copper hotspots and avoid probe diffusion within and/or out of the cell, coined as the copper-directed acyl imidazole (CDAI or CD) approach.[42,60] CD probes chelate labile copper, which then subsequently activates a proximal acyl imidazole electrophile by using the metal Lewis acid to withdraw electron density from the acyl group, making it susceptible to irreversible addition onto nucleophilic residues found in proteins and other biologically relevant macromolecules. This tandem activity-based sensing/labeling strategy can not only provide insight on the spatial localization of leached labile copper pools but also do so in an oxidation state-specific manner, as CD probes have been developed for the detection of labile Cu(I) and Cu(II) pools simultaneously[42] and for the oxidation state-specific detection of labile Cu(II).[60]

In this work, we employed two representative types of copper-containing nanoparticles that have been proposed as catalytic vectors in cancer therapy,[54,61] $CuFe_2O_4$[3,54] (herein, Cu−oxide) and copper hexacyanoferrate (Cu−HCF),[61,62] both of which contain leachable copper and are thus inherently toxic to cancer cells. Using activity-based sensing, we monitored their effects on labile copper status in cancer cells using two CD probes, one that is responsive to both Cu(I) and Cu(II) (CD664) and one that is responsive only to Cu(II) (CD649.2[60]). We observed that internalization of these nanoparticles significantly alter labile Cu(I)/Cu(II) homeostasis in a A549 lung cancer cell model with decreases in overall labile copper levels but increases in labile Cu(II) pools, which in turn affect metabolic pathways responsible for controlling GSH biosynthesis, Nuclear Factor-erythroid factor 2-related factor 2 (NRF2), and copper import/export trafficking pathways. Taken together, the results obtained provide valuable information into foundational biochemical mechanisms of action for ion-releasing catalytic metal nanoparticle therapeutics. More generally, this work also establishes the utility of activity-based sensing as a molecular imaging platform to inform the rational design of metal-based nanomedicines in the diagnosis and treatment of cancer and a broader array of diseases.

RESULTS AND DISCUSSION

Synthesis and Characterization of Therapeutic Copper Nanoparticles

We used copper oxides and hexacyanoferrates as representative examples of therapeutic copper-based nanoparticles,[3,54,61−63] both of which have been previously reported to undergo copper leaching during catalysis[54,62,64] and boast distinct copper coordination geometries. In the case of Cu−oxide, copper occupies tetrahedral sites surrounded by oxygen atoms (Figure 2a)[65] whereas copper occupies octahedral sites

https://doi.org/10.1021/cbmi.5c00237
Chem. Biomed. Imaging XXXX, XXX, XXX−XXX

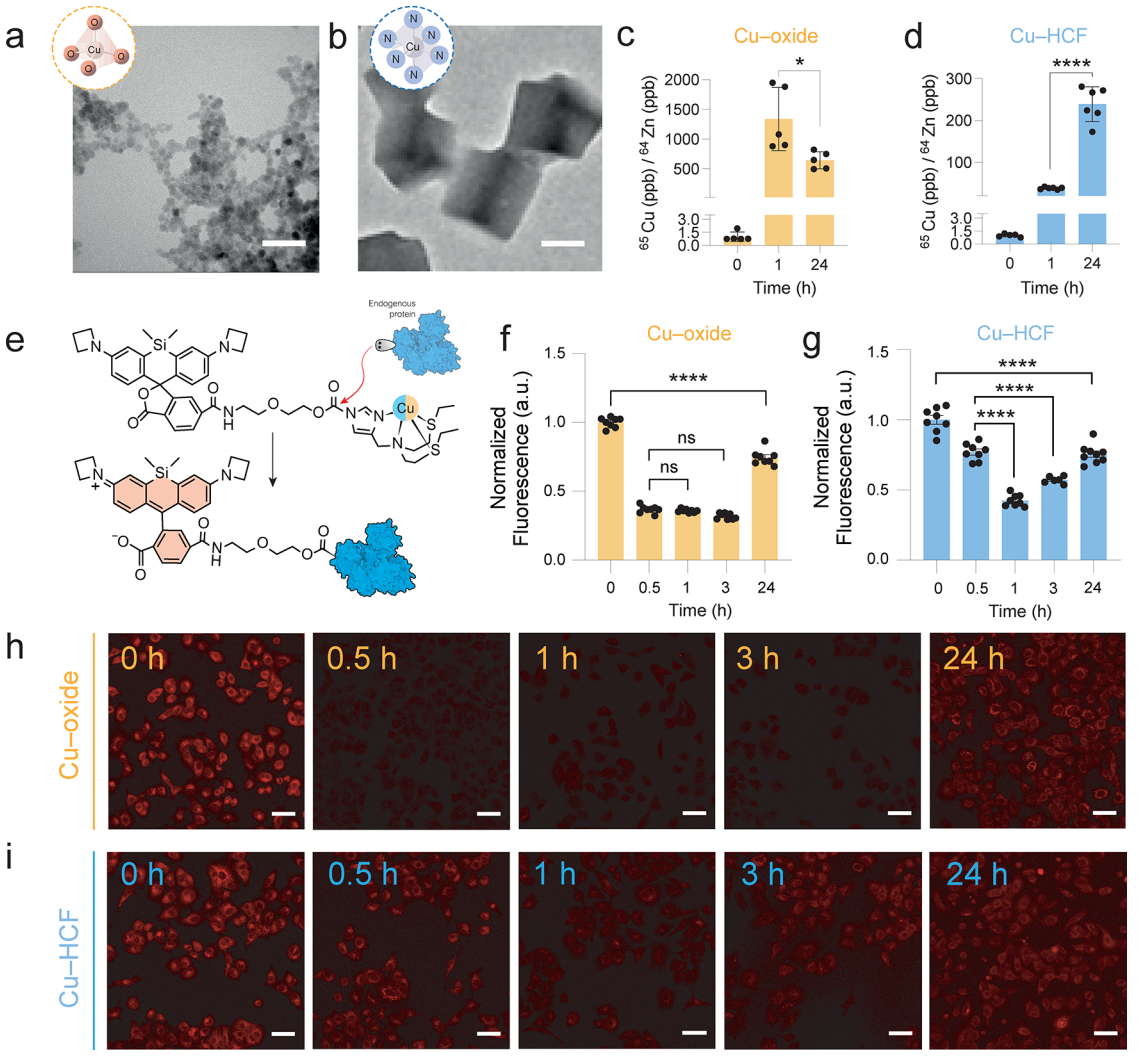

Figure 2. Copper coordination and TEM images of (a) Cu−oxide and (b) Cu−HCF nanoparticles employed in this study. Inset: (a) Cu−oxide and (b) Cu−HCF single nanoparticle at an enhanced resolution. Inset scale bar: 200 and 20 nm, respectively. ICP-MS analysis of A549 cells treated with (c) Cu−oxide and (d) Cu−HCF nanoparticles for 1 or 24 h reveals an increase in total copper levels upon nanoparticle treatment. Total cellular ^{65}Cu levels were normalized to total ^{64}Zn levels. Error bars denote SEM (n = 6). (e) Mechanism of action for the activity-based sensing probe CD664[42,60] to measure intracellular levels of labile copper. Binding of Cu(I) and/or Cu(II) Lewis acids to the N_2S_2 coordination pocket activates the pendant acyl imidazole electrophile for attack from nucleophilic residues from nearby proteins, anchoring the probe to the site of elevated labile copper. Quantification of CD664 fluorescence signal of A549 cells at different nanoparticle incubation times using (f) 6.25 μg Cu·mL^{-1} Cu−oxide and (g) 3.125 μg Cu·mL^{-1} Cu−HCF. (h, i) Confocal fluorescence images of CD664 in A549 cells treated with (h) Cu−oxide and (i) Cu−HCF. Early incubation times show a significant decrease in CD664 fluorescence as the cells appear to enter into a copper regulatory state where the metal nutrient is more tightly controlled and is less bioavailable within the cells. Fluorescence intensity of CD664 was determined from experiments with λ_{ex} = 633 nm. Scale bar = 50 μm. *P < 0.05, **P < 0.01, ***P < 0.001, and ****P < 0.0001; ns, not statistically significant. Error bars denote SEM (n = 8).

coordinated to nitrogen atoms in Cu−HCF (Figure 2b).[66] Oxide particles were synthesized via a hydrothermal method following our previous works.[54] Cu−HCF nanoparticles were synthesized via self-assembly mixing of Cu(II) with $Fe(CN)_6^{3-}$ ions in the presence of citric acid to modulate the particle size[61] (see Experimental Information for further details). Representative transmission electron microscopy (TEM) images of both nanoparticles are shown in Figure 2a-b, respectively. Oxide particles display a spherical morphology with an average diameter of 9.5 ± 1.0 nm (Figure S1), whereas Cu−HCF particles possess a cubic morphology with an average diameter of 80.0 ± 14.1 nm (Figure S1). XRD patterns of Cu−HCF confirmed the crystallinity of the sample with the coordination environment of Cu−N_6 and Fe−C_6 fitting well within the standard (JCPDS#02−0381) (Figure S2), while corresponding XRD pattern of $CuFe_2O_4$ matched with our previous works.[67] To validate that these nanoparticles undergo copper leaching, we performed elemental analysis on nanoparticle solutions after treatment with 5 mM GSH, which is abundant in the TME[3] and known to cause dissolution of copper-based nanoparticles.[54] Cu−oxide nanoparticles have a considerably smaller size, and therefore a larger external area per unit volume. However, both the copper leaching rate and total amount of copper released in a 24 h period were lower than those found for Cu−HCF (Figure S3). We suggest that the presence of vacancies typically present in Prussian Blue Analogues[68] as Cu−HCF together with the Jahn−Teller distortion induced by the Cu^{2+} in the nanostructure[69] (Figure

https://doi.org/10.1021/cbmi.5c00237
Chem. Biomed. Imaging XXXX, XXX, XXX−XXX

S4) may be responsible for the greater extent of copper dissolution displayed by the Cu−HCF nanoparticles. Based on these in vitro assays, we reasoned that intracellular copper ion release takes place to a higher extent for Cu−HCF nanoparticles. Both nanoparticles possess catalytic activity toward GSH depletion and are thus interesting candidates for catalytic nanomedicine therapy. In our previous work,[54] Cu−oxide nanoparticles showed a GSH depletion rate of 0.048 μmol GSH·min^{-1}·mg Cu^{-1} whereas Cu−HCF reached the value of 0.38 μmol GSH·min^{-1}·mg Cu^{-1} under physiological conditions (Figure S5). The higher GSH depletion rate relates to the faster copper release rate of Cu−HCF nanoparticles relative to the Cu−oxide congeners.[54]

Copper-Based Nanoparticle Treatment Decreases Overall Labile Copper Levels But Increases Labile Cu(II) Levels

We chose A549 cells as a model lung cancer cell line to study biochemical mechanisms of cellular responses to copper-based nanoparticle treatment and labile copper ion leaching. Previous reports suggest that A549 cells are resistant to treatment with elesclomol, a mitochondrial-targeted copper ionophore,[50] and CuO nanoparticles,[70] thus we hypothesized that these cells would display a fast and effective response against copper leaching. As a starting point, we studied the toxicity of the nanoparticles in A549 cells to determine a subcytotoxic dose to administer for further experiments (Figure S6). As expected, Cu−HCF was more toxic (CC_{50} = 5.66 μg Cu·mL^{-1}) than Cu−oxide (CC_{50} = 21.6 μg Cu·mL^{-1}), given the faster copper release for the former. At this point, we fixed the copper dose in subsequent experiments at 6.25 and 3.125 μg Cu·mL^{-1} for Cu−oxide and Cu−HCF, respectively; these doses ensured that cell viability was higher than 80% in both cases. We then quantified total internalized copper in A549 cells upon nanoparticle treatment using inductively coupled plasma mass spectrometry (ICP-MS) analysis (Figure 2c-d). Total copper levels in cells were significantly increased after 1 h, particularly in the case of Cu−oxide nanoparticles, as their smaller size likely results in a higher degree of internalization.[71] After 24 h of nanoparticle treatment, total copper levels decreased for cells exposed to Cu−oxide nanoparticles (Figure 2c), whereas total copper levels continued to increase for Cu−HCF nanoparticles (Figure 2d). While these data provide us with information on total copper status, it does not provide information on the bioavailability of the leached copper. Thus, we hypothesized that application of our recently developed tandem activity-based sensing and labeling probes could provide an effective means of measuring relative levels of labile Cu(I) and Cu(II) pools rather than total copper. This reasoning is supported by previous work from our laboratory using fluorescent copper sensors to identify intracellular accumulation of labile Cu(I) in response to contact killing of bacteria[72] and yeast[73] with antimicrobial copper surfaces. To meet this goal, activity-based sensing probes have been previously applied to successfully study changes in labile copper pools in these A549 cell models.[60] To investigate labile copper status upon nanoparticle treatment, we designed and synthesized the new activity-based sensing probe CD664 that bears a robust azetidine-based silicon rhodamine fluorophore scaffold.[74] CD664 is highly selective for labile copper over other biologically relevant metal ions but lacks oxidation state-specificity for Cu(I) vs Cu(II), and thus it can act as a tool for measuring total labile copper levels rather than a single oxidation state. The probe chelates labile copper via a favorable N_2S_2 ligand donor set (Figure 2e). CD664 was synthesized following a similar methodology as previously published[42] (see Experimental Information for further details). We investigated whether CD664 was capable of monitoring leached copper ions from both nanoparticles using A549 cell lysates to simulate labeling of the whole cellular proteome. Nanoparticles were preincubated with excess GSH for 24 h to ensure that majority of the leachable copper was released from the nanoparticles. Subsequently, this mixture was added to A549 cell lysate followed by CD664, and protein labeling was analyzed via sodium dodecyl sulfate−polyacrylamide gel electrophoresis (SDS-PAGE). In-gel fluorescence analysis revealed a dose-dependent increase in fluorescence for increasing concentration of either species of leached nanoparticle (Figure S7). These results validate CD664 as a fluorescent probe capable of analyzing labile copper derived from a nanoparticle. Fluorescence signals obtained using Cu−HCF nanoparticles were higher, in agreement with a greater extent of labile copper release (Figure S3). Interestingly, although both types of nanoparticles raised total amounts of intracellular copper and increased in vitro CD664 fluorescence, activity-based imaging with CD664 in live A549 cells shows that the labile copper pool rapidly decreases after treatment with either catalytic nanoparticle (Figure 2f-i, bright field images are found in Figures S8 and S9). Quantification of CD664 fluorescence signals revealed a fast and significant decrease in labile copper levels upon Cu−oxide treatment, in comparison to a more gradual depletion of labile copper pools for Cu−HCF (Figure 2f-g). Additionally, these effects are dose-dependent, as the CD664 fluorescence signal decreased more rapidly for treatment with Cu−oxide at higher concentrations, while the addition of lower amounts of Cu−oxide resulted in a more modest relative decrease in CD664 fluorescence signal (Figure S10 and Figure S11). Overall, the pattern of observed overall decreases in labile copper as directly imaged by CD664 suggests that the cell activates machinery to sequester and/or regulate labile copper pools triggered by the presence of leached copper ions derived from nanoparticle treatment. It is interesting to note that when these results are compared against analogous experiments with $CuCl_2$ as a soluble copper source, previously explored using activity-based sensing probes,[42,58,60] the opposite result was obtained, namely that such treatments led to an increase and expansion of the labile copper pool. Under native nutrient sensing conditions, copper ions are typically internalized into the cell through the high-affinity Cu(I)-selective copper ion channel/transporter CTR1,[75] where STEAP metalloreductases are required for internalization,[76] which allows for the precise control of copper uptake for a suitable metal homeostasis. DMT1 provides a complementary pathway for Cu(II) uptake.[60] In contrast, nanoparticle internalization typically occurs via endosome and eventual lysosome formation,[3,77,78] which produces a much faster rate of metal internalization and, simultaneously, a lack of oxidation state-specific regulation for the absorbed copper pool.

We posit that this rapid accumulation of copper upon nanoparticle treatment may elicit responses by the cell to counteract the disruption of its tightly regulated metal homeostasis. Indeed, while CD664 provides information on overall levels of labile copper, it does not discriminate against Cu(I) vs Cu(II). To confirm that the nanoparticles release Cu(I) in the presence of representative intracellular concentrations of GSH, we applied FCP-1, previously reported to

https://doi.org/10.1021/cbmi.5c00237
Chem. Biomed. Imaging XXXX, XXX, XXX−XXX

successfully monitor fluxes in intracellular labile Cu(I).[58] This probe contains three components: a red-emitting rhodamine (F_{576}) unit connected to a green-emitting (F_{526}) fluorescein moiety via a Tris(2-pyridylmethyl)amine (TPA) group; the TPA trigger is susceptible to Cu(I)-induced C−O oxidative bond cleavage (Figure S12a), providing an activity-based sensing approach to visualizing liable Cu(I) pools.[58,79] In the absence of Cu(I), the rhodamine group quenches the green emission from fluorescein via Förster Resonance Energy Transfer (FRET), leading to rhodamine-dominated red-shifted fluorescence, but in the presence of Cu(I), the bond between TPA and fluorescein is cleaved, disabling FRET (Figure S12a) and resulting in green fluorescein emission.[58] Therefore, the generation of Cu(I) species is related to an increase in the F_{526}/F_{576} ratio (Figure S12b). After incubation of either Cu−oxide and Cu−HCF nanoparticles with GSH to induce leaching and subsequent incubation with FCP-1, a rapid increase in the F_{526}/F_{576} ratio is observed, indicating a specific generation of Cu(I) during the leaching process (Figure S12c). Owing to the high intracellular GSH levels, Cu(I) is considered the predominant form of intracellular labile copper. However, recent work from our laboratory has also identified the existence of a labile Cu(II) pool and suggests that a heightened oxidative environment, such as that driven by oncogenes, can promote expansion of this pool.[60] Given the dynamic equilibrium that exists between these two forms of labile copper, we sought to study how internalization of copper-releasing particles affects labile copper pools in an oxidation state-specific manner. To this end, we selected the CD649.2 probe,[60] an activity-based sensor which replaces an ethylthioether ligand with a carboxylate group, which introduces a harder Lewis base into the coordination site of the first-generation CD649 probe. This substitution enhances the selectivity toward the harder Cu(II) Lewis acid over softer Cu(I) (Figure 3a).[60] Analogous to CD664, we validated the ability of CD649.2 to label proteins in the presence of leached Cu(II) with A549 cell lysates. Both nanoparticles produced an increase in CD649.2 fluorescence in the presence of A549 cell lysate, thereby confirming the capability of this probe to selectively track Cu(II) species generated from leached nanoparticles (Figure S13). We found a larger fluorescence turn-on response in the case of Cu−oxide nanoparticles, indicating a larger generation of Cu(II) from these particles.

Confocal imaging experiments with CD649.2 in live A549 cells reveal the generation of intracellular labile Cu(II) pools using both nanoparticles (Figure 3b-e and Figures S14 and S15). We found a higher CD649.2 fluorescence signal in the case of Cu−oxide nanoparticles, in agreement with protein labeling experiments (Figure S13). Treatment with Cu−oxide provokes an abrupt elevation of labile Cu(II) after 1 h of incubation, which slightly decreases after 24 h (Figure 3b-c), in agreement with the major changes found for CD664 (Figure 2f−g). This observation is in agreement with total copper decreasing at 24 h, as detected by ICP-MS (Figure 2c). On the other hand, cells treated with Cu−HCF nanoparticles display a continuous increase in CD649.2 signal after 1 and 24 h of incubation (Figure 3d-e), again tracking with the total copper increases measured by ICP-MS (Figure 2d).

Summarizing, the above results suggest that upon internalization, both nanoparticles leach copper, which is distributed in the form of labile Cu(II). To the best of our knowledge, activity-based sensing offers the first example of a method to directly monitor the redox status of labile metal ions leached

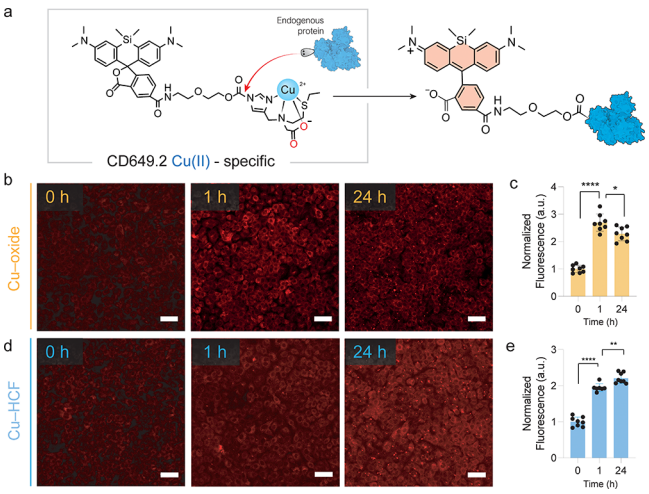

Figure 3. Cu(II)-specific probe CD649.2 with both copper and oxidation state specificity reveals an increase in labile Cu(II) pools in A549 cells following internalization of copper-based nanoparticles. (a) Mechanism of action for activity-based sensing of Cu(II) with the CD649.2 probe. Introducing a harder carboxylate Lewis base at the coordination site switches the selectivity of the probe to Cu(II)[60] while not compromising its capabilities to undergo nucleophilic conjugation with proteins in the same manner as CD664. (b, c) Confocal CD649.2 fluorescence images and quantification of A549 cells treated with 6.25 μg Cu·mL^{-1} Cu−oxide nanoparticles at different incubation times. Fluorescence quantification reveals a significant increase in labile Cu(II) after 1 and 24 h in comparison to the control. (d, e) Confocal CD649.2 fluorescence images and quantification of A549 cells treated with 3.125 μg Cu·mL^{-1} Cu−HCF nanoparticles at different incubation times. Fluorescence quantification reveals a time-dependent increase in labile Cu(II). Fluorescence intensity of CD649.2 was determined from experiments with λ_{ex} = 633 nm. Scale bar = 50 μm. *P < 0.05, **P < 0.01, ***P < 0.001, and ****P < 0.0001; ns, not statistically significant. Error bars denote SEM (n = 8).

from nanoparticles in a biological setting. Interestingly, the results suggest that internalization of copper-based nanoparticles reduce overall levels of labile copper in cells even though total copper levels increase. Moreover, upon further investigation, we find a relative elevation in labile Cu(II) with a shift in labile Cu(I)/Cu(II) ratios. Indeed, we observed distinct evolution patterns in total, overall labile, and oxidation state-specific labile copper pools depending on the nanoparticle used, in line with varying cellular responses to differences in nanoparticle internalization and labile copper ion leaching rates.

GSH and NRF2 Pathways Play Central Roles in Regulating Labile Copper Ion Pools Generated from Nanoparticle Treatment in Cells

Although treatment with copper nanoparticles induced an increase in labile Cu(II) pools, the overall labile copper content in cells was significantly decreased almost immediately upon nanoparticle incubation (Figure 2f-i). These observations indicate that a cellular response is occurring to counter this sudden metal imbalance. Given the established link between copper and cellular redox status,[58,60] we first sought to test whether this sudden increase in labile Cu(II) would lead to a heightened production of ROS. Indeed, Cu(II) has been widely explored in nanocatalytic therapy for its ability to deplete intracellular antioxidant reservoirs.[4] Along these lines, both Cu−oxide and Cu−HCF treatment induced a significant

https://doi.org/10.1021/cbmi.5c00237
Chem. Biomed. Imaging XXXX, XXX, XXX−XXX

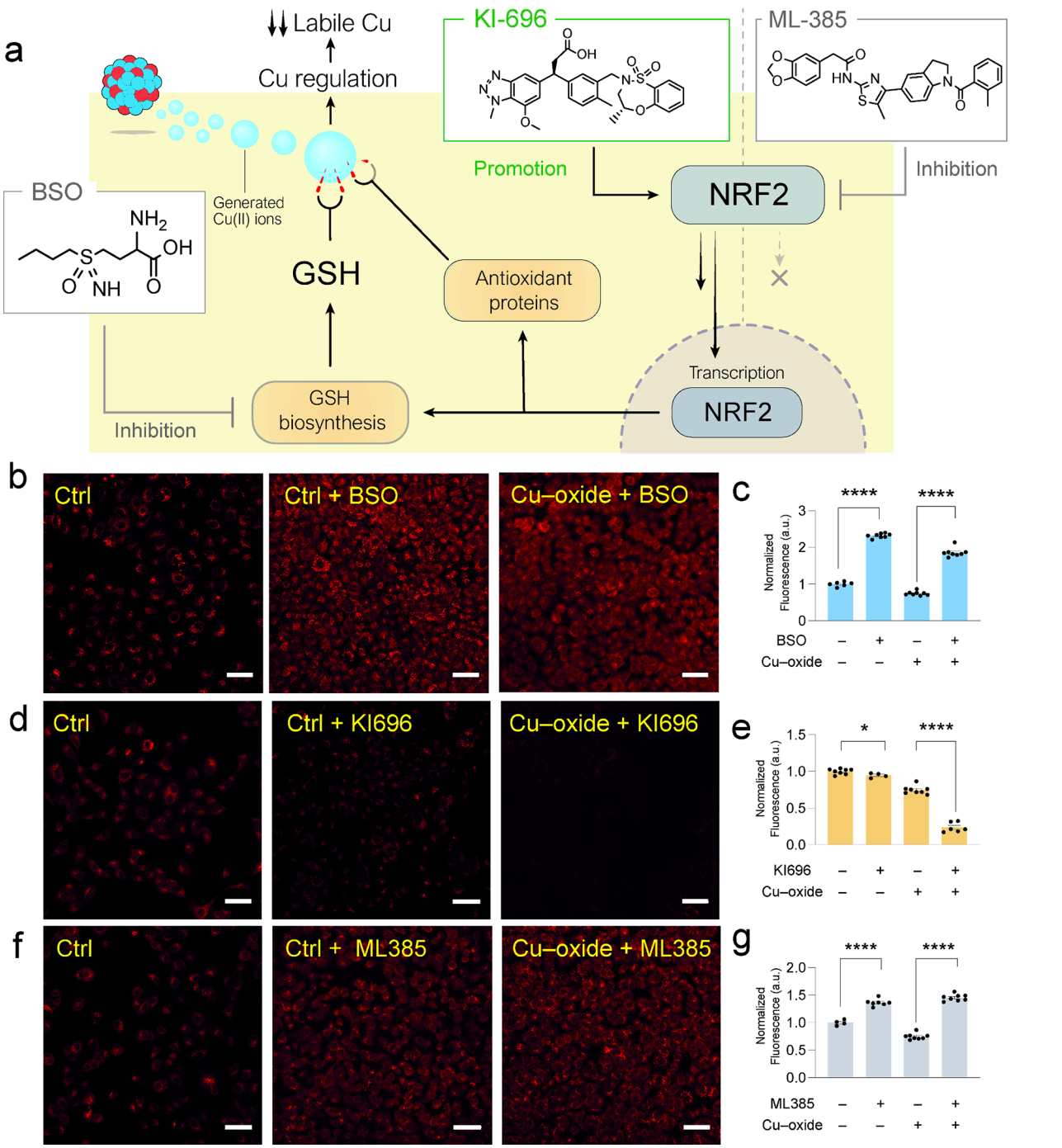

Figure 4. Pharmacological modulation of GSH biosynthesis and NRF2 activation pathways regulate maintenance of labile copper pools in cells following nanoparticle internalization. (a) Interplay between GSH and NRF2 pathways and labile copper ions generated from nanoparticle dissolution together with inhibitors and promoters employed in the study. GSH and NRF2 pathways can modulate overall labile copper levels through a variety of potential mechanisms. BSO blocks GSH biosynthesis[84] thereby reducing copper buffering and sequestration. KI696[87] and ML-385[88] promote or inhibit the antioxidant response element NRF2, decreasing or increasing overall labile copper levels, respectively. Labile copper imaging with the activity-based sensor CD664 in conjunction with these pharmacological treatments provides insights into how these biochemical pathways regulate labile copper ion pools released by nanoparticles. (b, c) Confocal CD664 fluorescence images and quantification of A549 cells treated with 0.5 mM BSO and 6.25 μg Cu·mL^{-1} of Cu−oxide for 24 h. Inhibition of GSH biosynthesis with BSO promotes the accumulation of intracellular labile copper pools. (d ,e) Confocal CD664 fluorescence images and quantification of A549 cells treated with 1 μM KI696 and 6.25 μg Cu·mL^{-1} of Cu−oxide for 24 h. Activation of the NRF2 pathway leads to a decrease in intracellular labile copper pools, as measured by CD664, likely due to upregulation in the expression of copper-sequestering proteins.[89] (f, g) Confocal fluorescence images and quantification of A549 cells treated with 10 μM ML385[87] and 6.25 μg Cu·mL^{-1} of Cu−oxide for 24 h. Inhibition of the NRF2 pathway prevents the upregulation of metal-buffering proteins in A549 cells, favoring an accumulation of labile copper after internalization of Cu−oxide nanoparticles. Fluorescence intensity of CD664 was determined from experiments with λ_{ex} = 633 nm. Scale bar = 50 μm. *P < 0.05, **P < 0.01, ***P < 0.001, and ****P < 0.0001; ns, not statistically significant. Error bars denote SEM (n = 8).

https://doi.org/10.1021/cbmi.5c00237
Chem. Biomed. Imaging XXXX, XXX, XXX−XXX

increase in the green fluorescence signal of CellROX, a broad-spectrum fluorescent ROS probe, in comparison to nontreated cells (Figure S16), confirming that nanoparticle incubation increases ROS in A549 cells. The released Cu(I) can also reduce endogenous H_2O_2, forming hydroxide and the highly oxidative hydroxyl radical species via Fenton-like chemistry.[9] In addition, the residual fraction of solid nanoparticle after labile copper leaching, mainly composed of FeO_x and $Fe(CN)_6$ units respectively, remained internalized in A549 cells as treatment with either nanoparticle increased total iron content, as shown by ICP-MS analysis (Figure S17). These species may also contribute to the generation of ROS due to their widely known Peroxidase-like activity[80,81] (i.e., oxidation of organic substrates using H_2O_2), which are especially active in mildly acidic intracellular environments such as lysosomes.[82]

In this context, cells typically increase their levels of the antioxidant buffering molecule GSH in response to an increase in oxidative stress, with previous reports indicating upregulation of GSH biosynthesis and regeneration in cancer models (Figure 4a).[7] Moreover, GSH is also involved in controlling the bioavailability of labile copper through a variety of mechanisms, including interactions with metallochaperones and metal-buffering proteins such as metallothionein.[58] GSH also has the potential to chelate copper directly, given its tight complex formation constant with Cu(I) ($\log K_f'=26.6$) measured in vitro,[54,83] but the direct evidence for physiological roles of cellular copper-GSH complexes remains elusive. We therefore explored whether GSH was involved in sequestering copper ions released from nanoparticles using buthionine sulfoximine (BSO), an inhibitor for the γ-glutamylcysteine synthetase (GCS) enzyme involved in the first step of GSH biosynthesis.[84] We hypothesized that if GSH could buffer labile copper pools, then depleting GSH levels would lead to an increase in overall labile copper levels upon nanoparticle treatment. To rule out the possibility that BSO can directly bind copper and itself lead to fluorescent changes under these experimental conditions, we investigated whether CD664, CD649.2 (Figure S18) or FCP-1 (Figure S19) were capable of monitoring the produced labile copper species after nanoparticle leaching in the presence or absence of BSO. We used A549 cell lysate to simulate labeling of the whole cellular proteome. Indeed, the fluorescence signals of CD664, CD649.2 or FCP-1 in this in vitro system containing Cu–oxide, Cu–HCF or $CuSO_4$ in the presence of 0.5 mM BSO were similar to treatments with the nanoparticles or $CuSO_4$ alone (Figures S18 and S19), indicating that BSO was not binding labile Cu(I) and Cu(II). After the treatment with BSO, the overall basal levels of labile copper in live A549 cells increased (Figure 4b), consistent with the role of GSH as a labile copper buffer in the cytosol[85,86] and in agreement with previous studies in HeLa cells.[58] Upon 24 h of incubation with 0.5 mM BSO and either Cu–oxide (Figure 4b-c, bright field images are shown in Figure S20) or Cu–HCF nanoparticles (Figure S21), we found significant increases in overall labile copper levels.

While these imaging results are in agreement with previous studies from our laboratory that link labile copper bioavailability with total GSH levels,[58] we found that labile copper levels in cells treated with BSO alone were still higher than in cells treated with BSO in conjunction with nanoparticles, suggest that additional pathways may be involved in regulating the nanoparticle-based copper influx. We speculated that the transcription factor NRF2 might be responsible, as it is activated upon disruption of GSH pools[90] and its activation leads to the upregulation of antioxidants and metal-buffering agents, including GSH[91] (Figure 4a). Cytosolic NRF2 levels are regulated by its interaction with the Kelch like-ECH-associated protein 1 (KEAP1)/Cullin3 system through ubiquitination.[92] When the interplay between KEAP1/Cullin3 and NRF2 is blocked, the entrance of NRF2 into the nuclei is favored, and consequently an upregulation in antioxidant and metal-buffering agents occurs which should directly affect labile copper levels in the cell.

To evaluate the interplay between labile copper pools and NRF2 status, we treated A549 cells with 1 μM of KI696, a potent and selective inhibitor of the KEAP1/NRF2 interaction. Analogous to control experiments with BSO, we demonstrated that KI696 also does not interfere with the copper responses of the activity-based sensing probes, as CD664, CD649.2 and FCP-1 fluorescence signals in the presence of KI696 and nanoparticles were similar to signals measured with nanoparticle treatments alone (Figures S18 and S19). KI696 acts effectively as a NRF2 promoter,[88] and we measured the effects of this pharmacological treatment on labile copper pools using CD664 imaging. As expected, in the absence of nanoparticle treatment, activation of the NRF2 pathway led to a decrease in overall basal labile copper levels (Figure 4d-e and Figure S20). However, cotreatment with Cu–oxide nanoparticles and KI696 provoked a significant decay in total labile copper levels that was significantly larger than treatment with Cu–oxide or KI696 alone, indicating that the NRF2 pathway plays a significant role in the cellular response to a sudden increase in copper levels upon nanoparticle treatment (Figure 4d-e and Figure S20). Correspondingly, we hypothesized that inhibition of the NRF2 pathway would block the upregulation of metal-buffering proteins and lead to an increase in labile copper pools. Indeed, we observed that upon incubation with 10 μM ML385, a potent NRF2 inhibitor[87] without copper-binding capabilities (Figures S18 and S19), that CD664 imaging shows an increase in overall basal labile copper levels, which was even higher in the presence of Cu–oxide nanoparticles (Figure 4f-g and Figure S20). Analogous results were obtained using Cu–HCF nanoparticles (Figure S21). These data provide further support that the NRF2 pathway as a key regulator of labile copper ion pools generated from nanoparticle leaching. Taken together, the results suggest that upon internalization of copper-containing nanoparticles and subsequent labile copper ion release, cells respond by promoting the NRF2 pathway to limit the bioavailability of labile copper.

Cells Respond to Internalization of Copper-Based Nanoparticles to Limit Copper Exposure via Regulating the Copper Exporter ATP7B and the Copper Importer CTR1

The fate of copper in cells is driven by dynamic and coordinated responses by copper storage, copper metallochaperone, and copper import/export and related transport proteins.[93] In this context, we tested the hypothesis that another possible explanation for the observed decrease in CD664 signal, indicating a loss of intracellular labile copper, could be attributed to changes in the expression of proteins that are involved in Cu import/export. In this context, ATP7B is a copper-dependent ATPase protein present in the membrane of the trans-Golgi network and is responsible for the metalation of proteins under basal levels of copper; however, upon exposure to elevated levels of copper, ATP7B is

https://doi.org/10.1021/cbmi.5c00237
Chem. Biomed. Imaging XXXX, XXX, XXX–XXX

trafficked toward the cell surface and toward lysosomal compartments[94] as a primary pathway for copper efflux.[53,95] Given that the vast majority of metal–based nanoparticles[96,97] are internalized via the endosomal-lysosomal pathway, we sought to quantify the protein expression of ATP7B in A549 cells upon exposure to Cu–oxide or Cu–HCF. Interestingly, Western Blot analysis (Figure 5a–c) revealed a drop in ATP7B expression after 1 h of treatment with Cu–oxide whereas expression did not change for Cu–HCF in the same early time frame (Figure 5c). ATP7B expression increased back to basal levels for both particles after a 24 h of treatment (Figure 5c), consistent with a compensatory cellular response to elevations the labile Cu(II) pools generated from nanoparticle internalization and leaching over these longer time scales (Figure 3).[98] We note that these finding complement work by Lu and colleagues,[56] who also detected a transient increase in ATP7B levels in hepatocyte cells treated with CuS nanoparticles, but its expression decayed after 1 h of treatment. These findings suggest a correlation between nanoparticle copper ion leaching rate and ATP7B expression. In addition, we also monitored the expression levels of high affinity copper uptake protein 1 (CTR1), the principal importer of extracellular Cu.[99] Incubation with either Cu–oxide did produce a significant downregulation of CTR1 expression in A549 cells within 1 h, which was maintained after 24 h of treatment for this particle (Figure 5b). In contrast, treatment with Cu–HCF did not alter CTR1 levels neither at 1 or 24 h, suggesting that the composition, internalization rate, and copper release kinetics of each specific nanoparticle can trigger different responses from the cell. In addition to its role as a copper nutrient importer, CTR1 can also act as a promoter of angiogenesis through activation of Vascular Endothelial Growth Factor receptor type 2 (VEGFR2).[100] Along these lines, CTR1 downregulation using copper-containing nanoparticles could also contribute to a reduced nutrient flux toward the TME.[101] These data reveal additional cellular response pathways toward copper-containing nanoparticle internalization, where the cell limits its copper exposure by upregulation of the ATP7B exporter to promote removal of excess labile copper ions generated after particle dissolution and the downregulation of CTR1 importer to decrease further copper ion uptake.

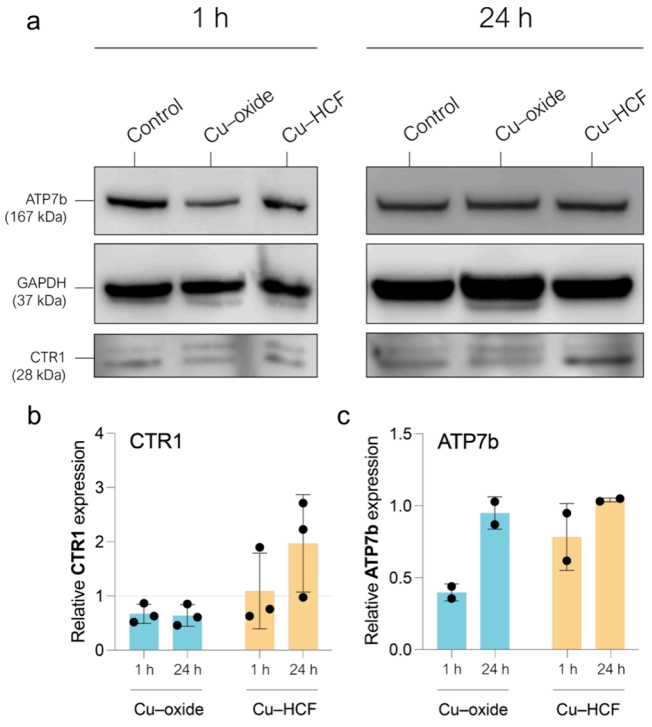

Figure 5. Copper-based nanoparticle internalization affects the regulation of cellular copper ion flux. (a) Western Blot analysis of ATP7B, CTR1, and Glyceraldehyde 3-phosphate dehydrogenase (GAPDH) proteins in A549 cells treated with 6.25 μg Cu·mL^{-1} Cu–oxide, 3.125 μg Cu·mL^{-1} Cu–HCF, or vehicle control for 1 or 24 h. Quantified (b) CTR1 and (c) ATP7b expression after incubation with Cu–oxide or Cu–HCF for 1 or 24 h. Error bars denote SEM. Full gel images are posted in the Supporting Information.

CONCLUDING REMARKS

We have established the utility of activity-based sensing as a method for applications in nanomedicine, by studying the biochemical mechanisms of redox and metal homeostasis in cells in response to treatment with anticancer metal-containing nanoparticle therapeutics. Using a pair of activity-based sensing probes that respond to either labile Cu(I) and Cu(II)

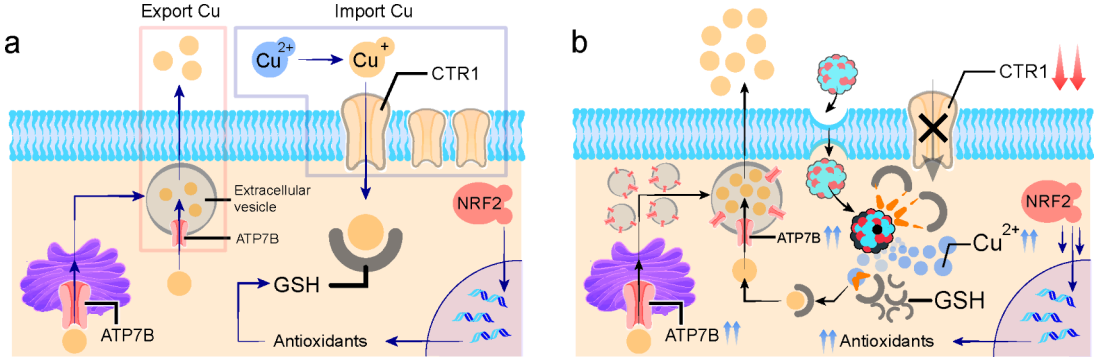

Figure 6. Schematic depiction of a model showing the effects of copper-based nanoparticles on copper homeostasis and compensatory biochemical responses in cells. (a) A basal, physiological scenario where copper and intracellular redox status are under normal and regulated homeostatic control. (b) A high-copper perturbation scenario following nanoparticle internalization and copper ion leaching where a significant pool of labile Cu(II) is generated. To overcome this acute or chronic aberrant exposure to excess of this metal and accompanying oxidative stress, cells sequester excess copper via GSH and NRF2 antioxidant pathways with concomitant upregulation of the copper ion export protein ATP7B to promote copper efflux and downregulation of the copper ion import protein CTR1 to block copper influx.

https://doi.org/10.1021/cbmi.5c00237
Chem. Biomed. Imaging XXXX, XXX, XXX–XXX

(CD664) or Cu(II) alone (CD649.2), we have studied the effects of therapeutic copper-leaching nanoparticles on labile copper levels and compensatory cellular responses in a lung cancer A549 cell model. Interestingly, although we observed that copper-containing nanomedicines increase the total copper content in cells as measured by ICP-MS (Figure 2c-d), internalization of copper-based nanoparticles results in a decrease in the overall levels of bioavailable labile copper pools (Figure 2f-i). This decrease in overall labile copper is accompanied by a shift in relative labile Cu(I)/Cu(II) ratios, as activity-based sensing using the oxidation state-selective probe CD649.2 revealed an accumulation of labile Cu(II) (Figure 3). In response to the increases in total copper and oxidized labile Cu(II), the cell triggers the activation of two distinct antioxidant pathways in response to oxidative stress, the elevation in bioavailability of the redox buffering molecule GSH and the activation of the redox-responsive transcription factor NRF2 (Figure 4). Moreover, the cell also responds to copper nanoparticle treatment via changes in metal homeostasis machinery, and regulates copper exposure by modifying the expression of ATP7B and CTR1 (Figure 6a, b).

Overall, this work provides insights into foundational biochemical mechanisms of how nanoparticles are able to release metal ions and influence metal homeostasis in living biological systems and compensatory cellular responses, particularly in the partitioning of total and labile metal ion pools and in the redox balance of metal oxidation states. Furthermore, our results establish that the activity-based sensing methodology can identify key factors to inform the future design of more effective nanoparticle-based platforms for nanomedicine. In the context of nanomedicine therapeutics for cancer, such strategies could involve combinatorial treatments of copper-leaching nanoparticles with relevant inhibitors to boost their efficiency toward selective killing of tumor cells versus healthy tissue. The growing connections between copper and cancer,[53] particularly in the discovery and emergence of novel pathways for copper-dependent cell proliferation (cuproplasia) and copper-dependent cell death (cuproptosis), presage a wealth of opportunities for nanomedicine to diagnose and treat metal-dependent disease vulnerabilities.

MATERIALS AND METHODS

Chemicals and Reagents

Reagents were purchased from commercial sources and used without further purification unless otherwise noted. Janelia Fluor 664, free acid was purchased from Tocris biotechne. Phosphate Buffer Saline (PBS without Ca and Mg, Corning), Dulbecco's Modified Eagle's Medium (DMEM, (GlutaMax)), Hanks' Balanced Salt Solution (HBSS + $CaCl_2$, + $MgCl_2$, Gibco), Cell Counting Kit-8 (CCK-8, Dojindo), CellROX-Green reagent (InvitroGen) were purchased from Thermo Fisher Scientific. The synthesis and characterization of materials has been performed by the Platform of Production of Biomaterials and Nanoparticles of the NANBIOSIS ICTS, more specifically by the Nanoparticle Synthesis Unit (Unit 9) of the CIBER in Bioengineering, Biomaterials & Nanomedicine (CIBER-BBN).

Instruments

Transmission electron microscopy (TEM) was performed using a FEI TECNAI T20 microscope operated at 200 keV. Confocal fluorescence imaging was performed with a Zeiss laser scanning microscope LSM880 with a 20× dry objective lens using Zen 2015 software (Carl Zeiss, Zen 2.3 black). X-ray diffraction (XRD) patterns were obtained in a PANalytical Empyrean equipment in Bragg–Brentano configuration using CuKα radiation and equipped with a PIXcel1D detector. Metal release from nanoparticles was measured using a 4100 Agilent MP-AES. Metarel content in cells was determined by measuring ^{65}Cu and ^{64}Zn using a Thermo Fisher iCAP-Qc ICP-MS in KED mode. Aristar BDH Ultra Concentrated nitric acid to dissolve samples was purchased from VWR. X-ray photoelectron spectroscopy (XPS) was performed with an Axis Supra spectrometer (Kratos Tech). The samples were mounted on a sample rod placed in the pretreatment chamber of the spectrometer and then evacuated at room temperature. The sample was excited by a monochromatized Al Kα source at 1486.6 eV and subsequently run at 8 kV and 15 mA. A survey spectrum was measured at 160 eV of pass energy, and for the individual peak regions, spectra were recorded with a pass energy of 20 eV. Analysis of the Cu 2p peak was performed with the CasaXPS software using a weighted sum of Lorentzian and Gaussian component.

Synthesis of Cu–Oxide

Copper–oxide was synthesized following previous works[54] without further modification.

Synthesis of Cu–HCF

Cu–HCF nanoparticle synthesis was adapted from the literature,[61] modifying the protocol to introduce Fe^{III} instead of Fe^{II}. 300 mg of citric acid (Sigma-Aldrich, 99.0%) and 36.8 mg of $K_3Fe(CN)_6$ were dissolved in 20 mL of distilled water. 10 mL of a 3.5 mg·mL^{-1} solution of $CuSO_4{\cdot}5H_2O$ was added dropwise to the previous solution. The mixture was left to stir overnight at room temperature. Final product was collected by centrifugation (two cycles of 10 000 rpm, 10 min) and stored at 4 °C for further use.

In Vitro Measurements of Copper Release from Nanoparticles

To a 5 mM GSH solution (pH = 7.4, buffered with HCO_3^-/CO_2), Cu–HCF nanoparticles were added until a final [Cu] = 0.1 mg·mL^{-1} was reached. 1 mL of solution was sampled and centrifuged at 13 300 rpm for 10 min. Supernatant was analyzed using MP-AES to quantify the released Cu.

GSH Oxidation Catalyzed by Cu–HCF

To a 0.1 M PBS solution, GSH and Cu–HCF catalyst were added to a final concentration of 4 mM and 0.01 mg Cu·mL^{-1}, respectively. Temperature was fixed at 37 °C. Samples were analyzed by UPLC-PDA following methodology from previous works[54] without further modification.

Cell Viability Assays

All cells used in this research were maintained by the UC Berkeley Tissue Culture Facility. A549 cells were seeded at 75% confluency in a 96-well cell plate. Cu–oxide and Cu–HCF nanoparticles from stock solution in PBS were added to DMEM to achieve a final concentration ranging from 0.00625 to 0.10 mg·mL^{-1}. Prior to the addition of the solution, nanoparticles were sonicated for 20 min. After 24 h, cells were washed with PBS (1×) and 100 μL of 10% v/v CCK-8 in DMEM solution was added to the well. Cells were then incubated at 37 °C in a 5% CO_2 incubator for 3 h. Finally, the absorbance at 450 nm was measured using a plate reader. Viability is presented as a percentage of control (n = 3 ± S.E.M).

ICP-MS Analysis

A549 cells were seeded in Falcon 6-well clear plates (ref. 353046) at 75% confluency. Cu–oxide and Cu–HCF nanoparticles resuspended in DMEM were added to a final concentration of 6.25 μg Cu·mL^{-1} and 3.15 μg Cu·mL^{-1}, respectively, and incubated for 1 and 24 h. Then, wells were washed with ice-cold PBS (1×) three times. Finally, 350 μL of concentrated nitric acid was added to the plate and incubated for 48 h at room temperature. Before analysis, 20 ppb of Ga was added to each sample as an internal standard. Results are expressed as an average ratio of [Cu]/[Zn] ± SEM (n = 6). Intracellular Zn concentration was used to normalize total cell number.

https://doi.org/10.1021/cbmi.5c00237
Chem. Biomed. Imaging XXXX, XXX, XXX–XXX

Synthesis of CD664

The complete synthetic route is shown in Figure S22. Methods are adapted from previous works.[42,60]

Synthesis of Compound 1

Sodium ethanethioate (727 mg, 8.65 mmol) and NaOH (188 mg, 4.71 mmol) were dissolved in 2 mL of MeOH through sonication and vigorous stirring for 30 min. Bis(2-chloroethyl)amine hydrochloride (701 mg, 3.93 mmol) was dissolved in 2.5 mL of MeOH and was slowly added to the previous solution. The mixture was stirred at room temperature overnight. MeOH was then removed under reduced pressure. The obtained slurry was extracted with hexane three times. The solution was filtered through a short plug of basic alumina and the filter was washed with DCM and ethyl acetate. Solvent was removed under reduced pressure and product was dried under high vacuum. ^{1}H NMR ($CDCl_3$, 400 MHz): δ 2.85 (t, J = 8 Hz, 4H, $NHCH_2$), 2.71 (t, J = 8 Hz, 4H, SCH_2), 2.55 (q, J = 8 Hz, 4H, SCH_2), 1.76 (s, broad, 1H, NH), 1.27 (t, J = 8 Hz, 6H, CH_3) (Figure S23).

Synthesis of Compound 2

4-Imidazole aldehyde (260 mg, 2.71 mmol) was dissolved in 1.40 mL of MeOH. Compound 1 (525 mg, 2.71 mmol) was dissolved in 7.2 mL of MeOH: Acetic acid mixture (10:1) and was slowly added to the previous solution. $NaBH_3CN$ (275 mg, 4.38 mmol) in 2 mL of MeOH was then added dropwise and stirred at room temperature overnight. N_2 was added to the solution and sealed with a septum. Reaction was quenched with 4−5 drops of HCl. Then, solvent was removed at high vacuum, extracted with DCM and dried with Na_2SO_4. Final product was purified with an alumina column (DCM: MeOH = 100:0 to 95:5). ^{1}H NMR ($CDCl_3$, 400 MHz): δ 7.70 (s, 1H, NCHN), 7.00 (s, 1H, CHN), 3.70 (s, 2H, NCH_2), 2.85 (t, J = 8 Hz, 4H, $NHCH_2$), 2.71 (t, J = 8 Hz, 4H, SCH_2), 2.55 (q, J = 8 Hz, 4H, SCH_2), 1.27 (t, J = 8 Hz, 6H, CH_3) (Figure S24).

Synthesis of Compound 3

A solution of *N*-(tert-butoxycarbonyl)-2-(2-aminoethoxy)ethanol (1.00 g, 4.74 mmol), N,N′-disuccinimidyl carbonate (2.50 g, 9.75 mmol), and triethylamine (0.98 g, 9.75 mmol) in CH_3CN (35 mL) was stirred for 2 h at 40 °C. After removal of the solvent by evaporation, the residue was dissolved in EtOAc. The organic layer was washed with sat. $NaHCO_3$ and dried over Na_2SO_4 followed by concentration in vacuo. The residue was purified by flash column chromatography on silica gel (EtOAc: Hexane = 50:50 to 75:25). ^{1}H NMR (400 MHz, $CDCl_3$) δ 4.47 (t, J = 4.8 Hz, 2H), 3.74 (t, J = 4.8 Hz, 2H), 3.56 (t, J = 4.8 Hz, 2H), 3.33 (m, 2H), 2.85 (s, 4H), 1.45 (s, 9H) (Figure S25).

Synthesis of Compound 4

A solution of compound 2 (315 mg, 1.15 mmol), 3 (329 mg, 0.95 mmol), and pyridine (223 μL, 2.81 mmol) in dry DMF (7.5 mL) was stirred at room temperature for 12 h under an N_2 atmosphere. The reaction was subsequently diluted with EtOAc, washed with water (×2) and brine, and then dried over Na_2SO_4, filtered, and evaporated. The crude residue was purified by column chromatography on silica gel (50−75% EtOAc/hexane, linear gradient) to yield the product (286.15 mg, 0.58 mmol, 61%) as a colorless oil. ^{1}H NMR ($CDCl_3$, 400 MHz) δ 8.09 (d, J = 1.3 Hz, 1H), 7.35 (d, J = 1.3 Hz, 1H), 4.86 (s, 1H), 4.54 (t, J = 4 Hz, 2H), 3.79 (t, J = 4 Hz, 2H), 3.68 (s, 2H), 3.57 (t, J = 5.4 Hz, 2H), 3.33 (t, J = 5.4 Hz, 2H), 2.80−2.72 (m, 4H), 2.71−2.63 (m, 4H), 2.55 (q, J = 7.4 Hz, 4H), 1.44 (s, 9H), 1.25 (t, J = 7.4 Hz, 6H). (Figure S26).

Synthesis of CD664

Compound 4 (12.4 mg, 24.6 μmol, 1.5 equiv) was dissolved in 5:1 DCM: TFA (1.20 mL: 0.25 mL) and stirred at room temperature for 30 min. Solvent was removed via rotary evaporation and residual TFA was removed by azeotroping 3 times with toluene (1.20 mL each time) and left under high vacuum for 30 min. Deprotected compound 4, Janelia Fluor 664, free acid (10.0 mg, 16.3 μmol), and DIPEA (22.0 μL, 131 μmol, 8.0 equiv) were then dissolved in dry DMF (1 mL). BOP (8.7 mg, 19.7 μmol, 1.2 equiv) was then added and the reaction was stirred at room temperature for 20 min. The product was then purified via prep-HPLC (conditions: 20% → 70% CH_3CN in H_2O with 10 mM NH_4OAc pH = 5 over 40 min and hold at 70% for another 40 min, 8 mL/min flow rate). HPLC fractions were combined and lyophilized to obtain a light blue powder (8.8 mg, 62%). UV−vis and MS spectra of the purified compound are shown in Figure S27. ^{1}H NMR (600 MHz, DMSO-d_6) δ 8.77 (t, J = 5.7 Hz, 1H), 8.14 (d, J = 1.3 Hz, 1H), 8.12 (d, J = 1.3 Hz, 1H), 8.03 (dd, J = 8.0, 1.3 Hz, 1H), 7.97 (d, J = 8.0 Hz, 1H), 7.65 (d, J = 1.3 Hz, 1H), 7.40 (d, J = 1.3 Hz, 1H), 6.70 (d, J = 2.6 Hz, 2H), 6.60 (d, J = 8.7 Hz, 2H), 6.30 (dd, J = 8.7, 2.6 Hz, 2H), 4.44 (t, J = 4.6 Hz, 2H), 3.81 (t, J = 7.3 Hz, 8H), 3.73 (t, J = 4.6 Hz, 2H), 3.57 − 3.55 (m, 4H), 3.39 (td, J = 11.5, 5.7 Hz, 2H), 2.63 − 2.55 (m, 8H), 2.47 (q, J = 7.3 Hz, 4H), 2.23 − 2.25 (m, 4H), 1.13 (t, J = 7.3 Hz, 6H), 0.59 (s, 3H), 0.48 (s, 3H). (Figure S26). ^{13}C NMR (600 MHz, DMSO-d_6) δ 169.2, 165.0, 154.6, 150.8, 148.2, 140.5, 139.8, 136.7, 135.7, 131.3, 128.1, 127.4, 125.4, 122.8, 115.4, 115.1, 112.6, 91.2, 68.5, 67.5, 67.0, 53.3, 51.9, 49.6, 28.6, 25.1, 16.3, 14.8, 0.0, −1.4. (Figure S29). HR-MS (ESI) m/z calculated for $[M + H]^+$ 883.370, found 883.371 (Figure S30).

Synthesis of CD649.2

The CD649.2 dye was synthesized following previous works[60] without further modification.

In Vitro Protein Labeling

To prepare cell lysate, A549 cells were seeded in Falcon 6-well clear plates (ref. 353046) at 75% confluency. Cells were washed using cold PBS (1×) twice. Cells were then collected using a cell scraper, and centrifuged at 6,000 rpm for 20 min at 4 °C. Supernatant was discarded and cell pellets were lysed with 150 μL of RIPA buffer (Thermo Scientific, 89900) with an added protease inhibitor cocktail (Roche, 05892953001) for 30 min. The protein concentrations were quantified by Pierce BCA assay (Thermo Scientific, 23250). To release all possible copper from either Cu−oxide or Cu−HCF, each nanoparticle (50 μg/mL) was incubated with 10 mM GSH in PBS (pH = 7.4, titrated with 1 M NaOH) for 24 h at 37 °C. Then, 2.40 μL of A549 cell lysate (5.2 mg·mL^{-1}) was preincubated with various concentrations of the nanoparticle + GSH mixture for 5 min at room temperature (diluted with PBS to a final volume of 24.5 μL). Finally, 0.5 μL of CD664 or CD649.2 (0.5 mM) was added to the previous solution and left to incubate for 1 h. The solution mixture was mixed with NuPAGE LDS Sample Buffer (4×) and heated at 95 °C for 5 min, followed by separation on Novex tris-glycine gels (Invitrogen) and scanned by ChemiDoc MP (Bio-Rad Laboratories, Inc.) for measuring in-gel fluorescence. The fluorescence was measured by 695/55 nm band-pass filter with excitation using red epi-illumination. The total protein level on the gel was then assayed by Coomassie Brilliant Blue R-250 (Biorad; 1610400) according to the manufacturer's protocol and scanned by ChemiDoc MP. The integrated intensities were analyzed by ImageLab.

Detection of Cu$^+$ Generation Using FCP-1

A solution containing 10 mM GSH and 50 μg·mL^{-1} of Cu−oxide or Cu−HCF was incubated in PBS (pH = 7.4, titrated with 1 M NaOH) for 24 h at 37 °C to induce the release of copper. Leached nanoparticles were then diluted into PBS with 40 vol % PEG-400 to a final concentration of 10 or 1 μg·mL^{-1} (final volume 999 μL). One μL of FCP-1 (5 mM) was then added to the solution and incubated for 1, 15, and 30 min, respectively. Finally, the fluorescence spectra of the solution were acquired using an excitation wavelength (λ_{exc} = 458 nm).

Confocal Fluorescence Imaging

A549 cells were seeded at 75% confluency in a poly L-lysine coated 8-well chamber slide (Nunc Lab-Tek). Cu−oxide and Cu−HCF nanoparticles resuspended in DMEM were added to a final concentration of 6.25 μg Cu·mL^{-1} and 3.125 μg Cu·mL^{-1}, respectively, and incubated for various times. Wells were then washed with HBSS once, and CD664 was added to a final concentration of 1

https://doi.org/10.1021/cbmi.5c00237
Chem. Biomed. Imaging XXXX, XXX, XXX−XXX

μM (0.6% of DMSO). Cells were incubated for 15 min at 37 °C in a 5% CO_2 incubator prior to imaging. CD664 was excited with a 633 nm laser, and the emissions were collected using a META detector between 650 and 750 nm. For CD649.2, cells were treated in the same way, however staining with CD649.2 was performed for 1 h and cells were then washed once with HBSS prior to imaging. All results are expressed considering average signal of control = 1 ± SEM (n = 8).

Detection of Labile Copper in the Presence of BSO, KI696, and ML385

We evaluated whether the labile copper detection properties of CD664, CD649.2, or FCP-1 were affected by the presence of BSO, KI696 or ML385. Cell lysates were prepared by seeding A549 cells in Falcon 6-well clear plates (ref.353046) at 75% confluency. Cells were washed using cold PBS (1×) twice. Cells were then collected using a cell scraper, and centrifuged at 6,000 rpm for 20 min at 4 °C. Supernatant was discarded and cell pellets were lysed with 150 μL of RIPA buffer (Thermo Scientific, 89900) with an added protease inhibitor cocktail (Roche, 05892953001) for 30 min. The protein concentrations were quantified by Pierce BCA assay (Thermo Scientific, 23250). To release all possible copper from either Cu−oxide or Cu−HCF, each nanoparticle (10 μg/mL) was incubated with 10 mM GSH in PBS (pH = 7.4, titrated with 1 M NaOH) and 0.5 mM BSO, 1 μM KI696 or 10 μM ML385 for 24 h at 37 °C. Then, 3.23 μL of A549 cell lysate (3.87 mg·mL^{-1}) was preincubated with the previous solutions for 5 min at room temperature (diluted with PBS to a final volume of 24.5 μL). Finally, 0.5 μL of CD664 or CD649.2 (0.5 mM) was added to the previous solution and left to incubate for 1 h. The solution mixture was mixed with NuPAGE LDS Sample Buffer (4×) and heated at 95 °C for 5 min, followed by separation on Novex tris-glycine gels (Invitrogen) and scanned by ChemiDoc MP (Bio-Rad Laboratories, Inc.) for measuring in-gel fluorescence. The fluorescence was measured by 695/55 nm band-pass filter with excitation using red epi-illumination. The total protein level on the gel was assayed by silver staining (ThermoFisher Scientific; 24612) according to the manufacturer's protocol and scanned by ChemiDoc MP. The integrated intensities were analyzed by ImageLab.

In the case of Cu^+, a solution containing 10 mM GSH and 1 μg·mL^{-1} of Cu−oxide or Cu−HCF was incubated in PBS (pH = 7.4, titrated with 1 M NaOH), to induce the release of copper, and 0.5 mM BSO, 1 μM KI696 or 10 μM ML385 for 24 h at 37 °C. Leached nanoparticles were then diluted into PBS with 40 vol % PEG-400 to a final concentration of 10 or 1 μg·mL^{-1} (final volume 999 μL). One μL of FCP-1 (5 mM) was then added to the solution and incubated 30 min, respectively. Finally, the fluorescence spectra of the solution were acquired using an excitation wavelength (λ_{exc} = 458 nm).

Image Analysis and Quantification

Nanoparticle diameter and confocal microscopy images of A549 cells were quantified using ImageJ software. Fluorescence intensity both of CD664 and CD649.2 was measured from two independent wells from a total of 8 pictures taken at x20 augments. For quantification, the area of stained cells was selected by fixing the appropriate threshold for each image with a Gaussian blur filter (sigma = 1). The "Create Mask" function followed by the "Create Selection" function were then used to create a selection from this threshold to finally quantify signal. Mean intensity of control samples was employed to perform the final statistic analysis using Prism7 (GraphPad).

Reactive Oxygen Species (ROS) Imaging

A549 cells were seeded at 60% of confluency in a poly L-lysine coated 8-well chamber slide (Nunc Lab-Tek). Cu−oxide and Cu−HCF nanoparticles resuspended in DMEM were added to a final concentration of 6.25 μg Cu·mL^{-1} and 3.125 μg Cu·mL^{-1}, respectively, and incubated for 1 or 24 h. Wells were washed with HBSS once, and then CellRox reagent was added to a final concentration of 5 μM (1% DMSO). Cells were incubated for 30 min at 37 °C in a 5% CO_2 incubator. Wells were then washed with HBSS twice, and fixed with paraformaldehyde (3.7%) for 15 min at 37 °C prior to imaging. CellROX was excited with 485 nm with an Ar laser, and the emissions were collected using a META detector between 500 and 540 nm. Results are normalized to control fluorescence = 1 ± SEM (n = 8).

Western Blot Analysis

10^6 A549 cells were seeded in a 6-well clear plates, and they were treated with Cu−oxide and Cu−HCF with a final concentration of 6.25 μg Cu·mL^{-1} and 3.125 μg Cu·mL^{-1}, respectively, and incubated for 1 or 24 h. Cells were washed using cold PBS (1×) twice and detached from the plate using TrypLE solution. Cell pellets were lysed with 150 μL of RIPA buffer (Thermo Scientific, 89900) with an added protease inhibitor cocktail (Roche, 05892953001) for 30 min under sonication at 4 °C. The protein concentrations were quantified by Pierce BCA assay (Thermo Scientific, 23250). 20 μg of protein per well were loaded onto an SDS−PAGE gel for 1 h at 200 V. After protein separation, dry transfer of proteins to a PVDF membrane was conducted using an iBLOT2 transfer instrument using the P0Method (20 V for 1 min, 23 V for 4 min and 25 V for 2 min). Then, membranes were blocked with Pierce Clear Milk Blocking Buffer (1x) for 1 h at room temperature, washed three times with PBS−T buffer and incubated with ATP7B and CTR1 antibodies overnight at 4 °C. After incubation, membrane was washed three times with PBS−T and incubated with GAPDH antibody for 1h at room temperature. Then, membrane was washed three times with PBS−T and incubated with secondary antibody (anti−Rb−HRP) (1:5000 dilution) for 1 h at room temperature. After incubation, membranes were washed three times with PBS−T and incubated for 1 min with HRP substrate. Chemiluminiscence images were captured using a ChemiDoc XRD+ system. GAPDH antibody was purchased from Cell Signaling Technologies (Asp175, no. 9661) and used with a dilution 1:1000. ATP7B antibody was purchased from Novus Biological (NB100−360) and used with a dilution of 1:1000. CTR1 antibody was purchased from Novus Biological (NBP2−36573) and used with a dilution of 1:100. Results are normalized by GAPDH expression.

Statistical Analysis

All the results are expressed as mean ± SEM. Statistical analysis of the biological experiments and the significant differences among the means were evaluated by two-way analysis of variance (ANOVA) for multiple comparisons by Dunnett's multiple comparisons test using GraphPad Software). Statistically significant differences were express as follows: *P < 0.05, **P < 0.005, ***P < 0.0005, and ****P < 0.00005.

■ ASSOCIATED CONTENT

Supporting Information

The Supporting Information is available free of charge at https://pubs.acs.org/doi/10.1021/cbmi.5c00237.

Figure S1, analysis of particle size of Cu−oxide and Cu−HCF nanoparticles. Figure S2, XRD pattern of Cu−HCF nanoparticles. Figure S3, time-lapse copper release from both nanoparticles after exposure to 5 mM GSH. Figure S4, XPS of the Cu $2p_{3/2}$ region of Cu−HCF. Figure S5, evolution of GSH concentration in the presence of Cu−HCF nanoparticles. Figure S6, cytotoxicity of Cu−oxide and Cu−HCF in A549 cells. Figure S7, in-gel detection of released Cu in A549 cell lysate using CD664. Figure S8, brightfield images of A549 cells treated with Cu−oxide at different times. Figure S9, brightfield images of A549 cells treated with Cu−HCF at different times. Figure S10, confocal microscopy images of A549 cells treated with varying concentrations of Cu−oxide nanoparticles. Figure S11, fluorescence quantification of CD664 in A549 incubated with different concentrations of Cu−oxide. Figure S12, detection of labile Cu(I) using FCP−1 in a test tube.

https://doi.org/10.1021/cbmi.5c00237
Chem. Biomed. Imaging XXXX, XXX, XXX−XXX

Figure S13, in-gel detection of released Cu in A549 cell lysate using CD649.2. Figure S14, brightfield images of A549 cells treated with Cu−oxide at different times for imaging with CD649.2. Figure S15, brightfield images of A549 cells treated with Cu−HCF at different times for imaging with CD649.2. Figure S16, quantification of ROS levels in treated A549 cells. Figure S17, quantification of intracellular Fe in treated A549 cells. Figure S18, in-gel detection of released Cu in A549 cell lysate using CD664 in the presence of BSO, KI696, and ML385. Figure S19, detection of labile Cu(I) using FCP−1 in a test tube in the presence of BSO, KI696, and ML385. Figure S20, brightfield images of A549 cells treated with Cu−oxide at different times for imaging with CD664 in the presence of BSO, KI696, and ML385. Figure S21, quantification of total labile Cu with CD664 in A549 cells treated with CuHCF and BSO, KI696, or ML385, respectively. Figure S22, synthetic route to synthesize CD664. Figures S23−S30, NMR and HRMS data (PDF)

AUTHOR INFORMATION

Corresponding Authors

Javier Bonet-Aleta − *Instituto de Nanociencia y Materiales de Aragon (INMA) CSIC-Universidad de Zaragoza, 50018 Zaragoza, Spain; Networking Res. Center in Biomaterials, Bioengineering and Nanomedicine (CIBER-BBN), Instituto de Salud Carlos III, 28029 Madrid, Spain; Department of Chemical and Environmental Engineering, University of Zaragoza, 50018 Zaragoza, Spain; Instituto de Investigación Sanitaria (IIS) de Aragón, 50009 Zaragoza, Spain; Department of Chemistry, University of California, Berkeley, California 94720, United States; Yusuf Hamied Department of Chemistry, University of Cambridge, CB2 1EW Cambridge, United Kingdom*; Email: jb2648@cam.ac.uk

Christopher J. Chang − *Department of Chemistry, University of California, Berkeley, California 94720, United States; Department of Chemistry, Princeton University, Princeton, New Jersey 08544, United States; Department of Molecular and Cell Biology and Helen Wills Neuroscience Institute, University of California, Berkeley, California 94720, United States; Chemical Sciences Division, Lawrence Berkeley National Laboratory, Berkeley, California 94720, United States*; orcid.org/0000-0001-5732-9497; Email: chrischang@princeton.edu

Authors

Aidan T. Pezacki − *Department of Chemistry, University of California, Berkeley, California 94720, United States; Department of Chemistry, Princeton University, Princeton, New Jersey 08544, United States*; orcid.org/0000-0002-7321-462X

Miku Oi − *Department of Chemistry, University of California, Berkeley, California 94720, United States*; orcid.org/0000-0002-9448-2375

Jose L. Hueso − *Instituto de Nanociencia y Materiales de Aragon (INMA) CSIC-Universidad de Zaragoza, 50018 Zaragoza, Spain; Networking Res. Center in Biomaterials, Bioengineering and Nanomedicine (CIBER-BBN), Instituto de Salud Carlos III, 28029 Madrid, Spain; Department of Chemical and Environmental Engineering, University of Zaragoza, 50018 Zaragoza, Spain; Instituto de Investigación Sanitaria (IIS) de Aragón, 50009 Zaragoza, Spain; Escuela Politécnica Superior, Universidad de Zaragoza, 22071 Huesca, Spain*; orcid.org/0000-0002-4546-4111

Jesus Santamaria − *Instituto de Nanociencia y Materiales de Aragon (INMA) CSIC-Universidad de Zaragoza, 50018 Zaragoza, Spain; Networking Res. Center in Biomaterials, Bioengineering and Nanomedicine (CIBER-BBN), Instituto de Salud Carlos III, 28029 Madrid, Spain; Department of Chemical and Environmental Engineering, University of Zaragoza, 50018 Zaragoza, Spain; Instituto de Investigación Sanitaria (IIS) de Aragón, 50009 Zaragoza, Spain*

Complete contact information is available at: https://pubs.acs.org/10.1021/cbmi.5c00237

Author Contributions

J.B.-A. and J.L.H. prepared and characterized the nanoparticles. J.B.-A., A.T.P., and M.O. synthesized CD664 and performed imaging experiments. J.B.-A., A.T.P., J.L.H., J.S., and C.J.C. designed the research. J.B.-A. and C.J.C wrote the manuscript with input from all authors. All authors have given approval to the final version of the manuscript.

Funding

C.J.C. thanks the NIH (GM79465, GM139245, and ES 28096) and the U.S. Department of Energy, Office of Science, Office of Advanced Scientific Computing, Office of Basic Energy Sciences, via the Division of Chemical Sciences, Geosciences, and Bioscience of the U.S. Department of Energy at Lawrence Berkeley National Laboratory (Grant No. DE-AC02-05CH11231) for support of the work. C.J.C. is a CIFAR Fellow. J.S. is thankful for the financial support from the European Research Council (ERC) Advanced Grant CADENCE number 742684. J.S. and J.L.H. acknowledge funding from the Spanish Research Agency (AEI) through Plan Nacional project CONCERT: PID2023-148732NB-I00 and Severo Ochoa Excellence Program: CEX2023-001286-S. J.B.-A. acknowledges the Spanish Government for a FPU predoctoral contract. J.B.-A. acknowledges financial support from the Herchel Smith Fund.

Notes

The authors declare no competing financial interest.

ACKNOWLEDGMENTS

We thank Alison Killilea and Willie S. Hercule (University of California, Berkeley Tissue Culture Facility) for expert technical assistance; Angel Gonzalez-Valero (University of California, Berkeley), Dan He (University of California, Berkeley), and Vanha Pham (University of California, Berkeley) for their support in Western Blot experiments; Leticia Sanchez-Uriel (University of Zaragoza) for her support in nanoparticle synthesis. The TEM measurements were conducted at the Laboratorio de Microscopias Avanzadas, Instituto de Nanociencia y Materiales de Aragon, Universidad de Zaragoza, Spain. The synthesis of materials has been performed by the Platform of Production of Biomaterials and Nanoparticles of the NANBIOSIS ICTS, more specifically by the Nanoparticle Synthesis Unit of the CIBER in BioEngineering, Biomaterials & Nanomedicine (CIBER-BBN). The 600 MHz cryoprobe was funded by the NIH grant S10OD024998. J.L.H. and J.S. also thank the InterPHOT thematic network and "Conexion Fotocatalisis" CSIC hub.

https://doi.org/10.1021/cbmi.5c00237
Chem. Biomed. Imaging XXXX, XXX, XXX−XXX

REFERENCES

(1) Wang, X.; Zhong, X.; Liu, Z.; Cheng, L. Recent progress of chemodynamic therapy-induced combination cancer therapy. *Nano Today* **2020**, *35*, 100946.

(2) Chen, J.; Zhu, Y.; Wu, C.; Shi, J. Nanoplatform-based cascade engineering for cancer therapy. *Chem. Soc. Rev.* **2020**, *49* (24), 9057−9094.

(3) Bonet-Aleta, J.; Sancho-Albero, M.; Calzada-Funes, J.; Irusta, S.; Martin-Duque, P.; Hueso, J. L.; Santamaria, J. Glutathione-Triggered catalytic response of Copper-Iron mixed oxide Nanoparticles. Leveraging tumor microenvironment conditions for chemodynamic therapy. *J. Colloid Interface Sci.* **2022**, *617*, 704−717.

(4) Ding, Y.; Dai, Y.; Wu, M.; Li, L. Glutathione-mediated nanomedicines for cancer diagnosis and therapy. *Chem. Eng. J.* **2021**, *426*, 128880.

(5) López-Lázaro, M. Dual role of hydrogen peroxide in cancer: Possible relevance to cancer chemoprevention and therapy. *Cancer Letters* **2007**, *252* (1), 1−8.

(6) Burdon, R. H. Superoxide and hydrogen peroxide in relation to mammalian cell proliferation. *Free Radic. Biol. Med.* **1995**, *18* (4), 775−794.

(7) Harris, I. S.; Treloar, A. E.; Inoue, S.; Sasaki, M.; Gorrini, C.; Lee, K. C.; Yung, Ka Y.; Brenner, D.; Knobbe-Thomsen, C. B.; Cox, M. A.; et al. Glutathione and Thioredoxin Antioxidant Pathways Synergize to Drive Cancer Initiation and Progression. *Cancer Cell* **2015**, *27* (2), 211−222.

(8) Lin, L.-S.; Huang, T.; Song, J.; Ou, X.-Y.; Wang, Z.; Deng, H.; Tian, R.; Liu, Y.; Wang, J.-F.; Liu, Y.; et al. Synthesis of Copper Peroxide Nanodots for H2O2 Self-Supplying Chemodynamic Therapy. *J. Am. Chem. Soc.* **2019**, *141* (25), 9937−9945.

(9) Ma, B.; Wang, S.; Liu, F.; Zhang, S.; Duan, J.; Li, Z.; Kong, Y.; Sang, Y.; Liu, H.; Bu, W.; Li, L. Self-Assembled Copper-Amino Acid Nanoparticles for in Situ Glutathione "AND" H2O2 Sequentially Triggered Chemodynamic Therapy. *J. Am. Chem. Soc.* **2019**, *141* (2), 849−857.

(10) Lu, X.; Gao, S.; Lin, H.; Yu, L.; Han, Y.; Zhu, P.; Bao, W.; Yao, H.; Chen, Y.; Shi, J. Bioinspired Copper Single-Atom Catalysts for Tumor Parallel Catalytic Therapy. *Adv. Mater.* **2020**, *32* (36), 2002246.

(11) Huo, M.; Wang, L.; Chen, Y.; Shi, J. Tumor-selective catalytic nanomedicine by nanocatalyst delivery. *Nat. Commun.* **2017**, *8* (1), 357.

(12) Yang, B.; Yao, H.; Tian, H.; Yu, Z.; Guo, Y.; Wang, Y.; Yang, J.; Chen, C.; Shi, J. Intratumoral synthesis of nano-metalchelate for tumor catalytic therapy by ligand field-enhanced coordination. *Nat. Commun.* **2021**, *12* (1), 3393.

(13) Lin, L.-S.; Song, J.; Song, L.; Ke, K.; Liu, Y.; Zhou, Z.; Shen, Z.; Li, J.; Yang, Z.; Tang, W.; et al. Simultaneous Fenton-like Ion Delivery and Glutathione Depletion by MnO2-Based Nanoagent to Enhance Chemodynamic Therapy. *Angew. Chem., Int. Ed.* **2018**, *57* (18), 4902−4906.

(14) Wu, F.; Du, Y.; Yang, J.; Shao, B.; Mi, Z.; Yao, Y.; Cui, Y.; He, F.; Zhang, Y.; Yang, P. Peroxidase-like Active Nanomedicine with Dual Glutathione Depletion Property to Restore Oxaliplatin Chemosensitivity and Promote Programmed Cell Death. *ACS Nano* **2022**, *16* (3), 3647−3663.

(15) Yang, B.; Chen, Y.; Shi, J. Nanocatalytic Medicine. *Adv. Mater.* **2019**, *31* (39), No. e1901778.

(16) Tang, Z.; Zhao, P.; Wang, H.; Liu, Y.; Bu, W. Biomedicine Meets Fenton Chemistry. *Chem. Rev.* **2021**, *121* (4), 1981−2019.

(17) Koo, S.; Park, O. K.; Kim, J.; Han, S. I.; Yoo, T. Y.; Lee, N.; Kim, Y. G.; Kim, H.; Lim, C.; Bae, J.-S.; et al. Enhanced Chemodynamic Therapy by Cu-Fe Peroxide Nanoparticles: Tumor Microenvironment-Mediated Synergistic Fenton Reaction. *ACS Nano* **2022**, *16* (2), 2535−2545.

(18) Garcia-Peiro, J. I.; Bonet-Aleta, J.; Santamaria, J.; Hueso, J. L. Platinum nanoplatforms: classic catalysts claiming a prominent role in cancer therapy. *Chem. Soc. Rev.* **2022**, *51* (17), 7662−7681.

(19) Gao, S.; Lin, H.; Zhang, H.; Yao, H.; Chen, Y.; Shi, J. Nanocatalytic Tumor Therapy by Biomimetic Dual Inorganic Nanozyme-Catalyzed Cascade Reaction. *Adv. Sci.* **2019**, *6* (3), 1801733.

(20) Zhao, P.; Li, H.; Bu, W. A Forward Vision for Chemodynamic Therapy: Issues and Opportunities. *Angew. Chem., Int. Ed.* **2023**, *62* (7), No. e202210415.

(21) Francia, V.; Reker-Smit, C.; Salvati, A. Mechanisms of Uptake and Membrane Curvature Generation for the Internalization of Silica Nanoparticles by Cells. *Nano Lett.* **2022**, *22* (7), 3118−3124.

(22) Donahue, N. D.; Acar, H.; Wilhelm, S. Concepts of nanoparticle cellular uptake, intracellular trafficking, and kinetics in nanomedicine. *Adv. Drug Delivery Rev.* **2019**, *143*, 68−96.

(23) Soenen, S. J.; Parak, W. J.; Rejman, J.; Manshian, B. (Intra)Cellular Stability of Inorganic Nanoparticles: Effects on Cytotoxicity, Particle Functionality, and Biomedical Applications. *Chem. Rev.* **2015**, *115* (5), 2109−2135.

(24) Liu, J.; Yuan, Y.; Cheng, Y.; Fu, D.; Chen, Z.; Wang, Y.; Zhang, L.; Yao, C.; Shi, L.; Li, M.; et al. Copper-Based Metal-Organic Framework Overcomes Cancer Chemoresistance through Systemically Disrupting Dynamically Balanced Cellular Redox Homeostasis. *J. Am. Chem. Soc.* **2022**, *144* (11), 4799−4809.

(25) Zhou, M.; Tian, M.; Li, C. Copper-Based Nanomaterials for Cancer Imaging and Therapy. *Bioconj. Chem.* **2016**, *27* (5), 1188−1199.

(26) Aishajiang, R.; Liu, Z.; Wang, T.; Zhou, L.; Yu, D. Recent Advances in Cancer Therapeutic Copper-Based Nanomaterials for Antitumor Therapy. *Molecules* **2023**, *28* (5), 2303.

(27) Zhong, X.; Dai, X.; Wang, Y.; Wang, H.; Qian, H.; Wang, X. Copper-based nanomaterials for cancer theranostics. *Wiley Interdiscip. Rev. Nanomed. Nanobiotechnol.* **2022**, *14* (4), No. e1797.

(28) Lippard, S. J.; Berg, J. M.; Klatt, G. *Principles of Bioinorganic Chemistry*; University Science Books, 1994.

(29) Lancaster, K. M.; DeBeer George, S.; Yokoyama, K.; Richards, J. H.; Gray, H. B. Type-zero copper proteins. *Nat. Chem.* **2009**, *1* (9), 711−715.

(30) Solomon, E. I.; Heppner, D. E.; Johnston, E. M.; Ginsbach, J. W.; Cirera, J.; Qayyum, M.; Kieber-Emmons, M. T.; Kjaergaard, C. H.; Hadt, R. G.; Tian, L. Copper Active Sites in Biology. *Chem. Rev.* **2014**, *114* (7), 3659−3853.

(31) Guengerich, F. P. Introduction to Metals in Biology 2018: Copper homeostasis and utilization in redox enzymes. *J. Biol. Chem.* **2018**, *293* (13), 4603−4605.

(32) Gaggelli, E.; Kozlowski, H.; Valensin, D.; Valensin, G. Copper homeostasis and neurodegenerative disorders (Alzheimer's, prion, and Parkinson's diseases and amyotrophic lateral sclerosis). *Chem. Rev.* **2006**, *106* (6), 1995−2044.

(33) Adam, S. M.; Wijeratne, G. B.; Rogler, P. J.; Diaz, D. E.; Quist, D. A.; Liu, J. J.; Karlin, K. D. Synthetic Fe/Cu Complexes: Toward Understanding Heme-Copper Oxidase Structure and Function. *Chem. Rev.* **2018**, *118* (22), 10840−11022.

(34) Chang, C. J. Searching for harmony in transition-metal signaling. *Nat. Chem. Biol.* **2015**, *11* (10), 744−747.

(35) Chang, C. J. Bioinorganic Life and Neural Activity: Toward a Chemistry of Consciousness? *Acc. Chem. Res.* **2017**, *50* (3), 535−538.

(36) Ackerman, C. M.; Chang, C. J. Copper signaling in the brain and beyond. *J. Biol. Chem.* **2018**, *293* (13), 4628−4635.

(37) Tsang, T.; Davis, C. I.; Brady, D. C. Copper biology. *Curr. Biol.* **2021**, *31* (9), R421−r427.

(38) Pham, V. N.; Chang, C. J. Metalloallostery and Transition Metal Signaling: Bioinorganic Copper Chemistry Beyond Active Sites. *Angew. Chem., Int. Ed.* **2023**, *62* (11), No. e202213644.

(39) Dodani, S. C.; Domaille, D. W.; Nam, C. I.; Miller, E. W.; Finney, L. A.; Vogt, S.; Chang, C. J. Calcium-dependent copper redistributions in neuronal cells revealed by a fluorescent copper sensor and X-ray fluorescence microscopy. *Proc. Natl. Acad. Sci. U. S. A.* **2011**, *108* (15), 5980−5985.

(40) Dodani, S. C.; Firl, A.; Chan, J.; Nam, C. I.; Aron, A. T.; Onak, C. S.; Ramos-Torres, K. M.; Paek, J.; Webster, C. M.; Feller, M. B.;

https://doi.org/10.1021/cbmi.5c00237
Chem. Biomed. Imaging XXXX, XXX, XXX−XXX

Chang, C. J. Copper is an endogenous modulator of neural circuit spontaneous activity. *Proc. Natl. Acad. Sci. U. S. A.* **2014**, *111* (46), 16280−16285.
(41) Xiao, T.; Ackerman, C. M.; Carroll, E. C.; Jia, S.; Hoagland, A.; Chan, J.; Thai, B.; Liu, C. S.; Isacoff, E. Y.; Chang, C. J. Copper regulates rest-activity cycles through the locus coeruleus-norepinephrine system. *Nat. Chem. Biol.* **2018**, *14* (7), 655−663.
(42) Lee, S.; Chung, C. Y.-S.; Liu, P.; Craciun, L.; Nishikawa, Y.; Bruemmer, K. J.; Hamachi, I.; Saijo, K.; Miller, E. W.; Chang, C. J. Activity-Based Sensing with a Metal-Directed Acyl Imidazole Strategy Reveals Cell Type-Dependent Pools of Labile Brain Copper. *J. Am. Chem. Soc.* **2020**, *142* (35), 14993−15003.
(43) Krishnamoorthy, L.; Cotruvo, J. A.; Chan, J.; Kaluarachchi, H.; Muchenditsi, A.; Pendyala, V. S.; Jia, S.; Aron, A. T.; Ackerman, C. M.; Wal, M. N. V.; et al. Copper regulates cyclic-AMP-dependent lipolysis. *Nat. Chem. Biol.* **2016**, *12* (8), 586−592.
(44) Brady, D. C.; Crowe, M. S.; Turski, M. L.; Hobbs, G. A.; Yao, X.; Chaikuad, A.; Knapp, S.; Xiao, K.; Campbell, S. L.; Thiele, D. J.; Counter, C. M. Copper is required for oncogenic BRAF signalling and tumorigenesis. *Nature* **2014**, *509* (7501), 492−496.
(45) Tsang, T.; Posimo, J. M.; Gudiel, A. A.; Cicchini, M.; Feldser, D. M.; Brady, D. C. Copper is an essential regulator of the autophagic kinases ULK1/2 to drive lung adenocarcinoma. *Nat. Cell Biol.* **2020**, *22* (4), 412−424.
(46) Guo, J.; Cheng, J.; Zheng, N.; Zhang, X.; Dai, X.; Zhang, L.; Hu, C.; Wu, X.; Jiang, Q.; Wu, D.; et al. Copper Promotes Tumorigenesis by Activating the PDK1-AKT Oncogenic Pathway in a Copper Transporter 1 Dependent Manner. *Adv. Sci.* **2021**, *8* (18), 2004303.
(47) Chojnowski, J. E.; Li, R.; Tsang, T.; Alfaran, F. H.; Dick, A.; Cocklin, S.; Brady, D. C.; Strochlic, T. I. Copper Modulates the Catalytic Activity of Protein Kinase CK2. *Front Mol. Biosci* **2022**, *9*, 878652.
(48) Turski, M. L.; Brady, D. C.; Kim, H. J.; Kim, B.-E.; Nose, Y.; Counter, C. M.; Winge, D. R.; Thiele, D. J. A Novel Role for Copper in Ras/Mitogen-Activated Protein Kinase Signaling. *Mol. Cell. Biol.* **2012**, *32* (7), 1284−1295.
(49) Que, E. L.; Domaille, D. W.; Chang, C. J. Metals in Neurobiology: Probing Their Chemistry and Biology with Molecular Imaging. *Chem. Rev.* **2008**, *108* (5), 1517−1549.
(50) Tsvetkov, P.; Coy, S.; Petrova, B.; Dreishpoon, M.; Verma, A.; Abdusamad, M.; Rossen, J.; Joesch-Cohen, L.; Humeidi, R.; Spangler, R. D.; et al. Copper induces cell death by targeting lipoylated TCA cycle proteins. *Science* **2022**, *375* (6586), 1254−1261.
(51) Ackerman, C. M.; Lee, S.; Chang, C. J. Analytical Methods for Imaging Metals in Biology: From Transition Metal Metabolism to Transition Metal Signaling. *Anal. Chem.* **2017**, *89* (1), 22−41.
(52) Hare, D. J.; New, E. J.; de Jonge, M. D.; McColl, G. Imaging metals in biology: balancing sensitivity, selectivity and spatial resolution. *Chem. Soc. Rev.* **2015**, *44* (17), 5941−5958.
(53) Ge, E. J.; Bush, A. I.; Casini, A.; Cobine, P. A.; Cross, J. R.; DeNicola, G. M.; Dou, Q. P.; Franz, K. J.; Gohil, V. M.; Gupta, S.; et al. Connecting copper and cancer: from transition metal signalling to metalloplasia. *Nat. Rev. Cancer* **2022**, *22* (2), 102−113.
(54) Bonet-Aleta, J.; Encinas-Gimenez, M.; Urriolabeitia, E.; Martin-Duque, P.; Hueso, J. L.; Santamaria, J. Unveiling the interplay between homogeneous and heterogeneous catalytic mechanisms in copper-iron nanoparticles working under chemically relevant tumour conditions. *Chem. Sci.* **2022**, *13* (28), 8307−8320.
(55) Liu, C.; Wang, D.; Zhang, S.; Cheng, Y.; Yang, F.; Xing, Y.; Xu, T.; Dong, H.; Zhang, X. Biodegradable Biomimic Copper/Manganese Silicate Nanospheres for Chemodynamic/Photodynamic Synergistic Therapy with Simultaneous Glutathione Depletion and Hypoxia Relief. *ACS Nano* **2019**, *13* (4), 4267−4277.
(56) Wang, X.; Guo, L.; Zhang, S.; Chen, Y.; Chen, Y.-T.; Zheng, B.; Sun, J.; Qian, Y.; Chen, Y.; Yan, B.; Lu, W. Copper Sulfide Facilitates Hepatobiliary Clearance of Gold Nanoparticles through the Copper-Transporting ATPase ATP7B. *ACS Nano* **2019**, *13* (5), 5720−5730.
(57) Chan, J.; Dodani, S. C.; Chang, C. J. Reaction-based small-molecule fluorescent probes for chemoselective bioimaging. *Nat. Chem.* **2012**, *4* (12), 973−984.
(58) Chung, C. Y.-S.; Posimo, J. M.; Lee, S.; Tsang, T.; Davis, J. M.; Brady, D. C.; Chang, C. J. Activity-based ratiometric FRET probe reveals oncogene-driven changes in labile copper pools induced by altered glutathione metabolism. *Proc. Natl. Acad. Sci. U.S.A.* **2019**, *116* (37), 18285−18294.
(59) Bruemmer, K. J.; Crossley, S. W. M.; Chang, C. J. Activity-Based Sensing: A Synthetic Methods Approach for Selective Molecular Imaging and Beyond. *Angew. Chem., Int. Ed.* **2020**, *59* (33), 13734−13762.
(60) Pezacki, A. T.; Matier, C. D.; Gu, X.; Kummelstedt, E.; Bond, S. E.; Torrente, L.; Jordan-Sciutto, K. L.; DeNicola, G. M.; Su, T. A.; Brady, D. C.; Chang, C. J. Oxidation state-specific fluorescent copper sensors reveal oncogene-driven redox changes that regulate labile copper(II) pools. *Proc. Natl. Acad. Sci. U.S.A.* **2022**, *119* (43), No. e2202736119.
(61) Wang, D.; Wu, H.; Wang, C.; Gu, L.; Chen, H.; Jana, D.; Feng, L.; Liu, J.; Wang, X.; Xu, P.; et al. Self-Assembled Single-Site Nanozyme for Tumor-Specific Amplified Cascade Enzymatic Therapy. *Angew. Chem., Int. Ed.* **2021**, *60* (6), 3001−3007.
(62) Bonet-Aleta, J.; Hueso, J. L.; Valls-Chiva, A.; Ruiz-Aranda, I.; Manzanilla, B.; Garcia-Peiro, J. I.; Aina, S.; Urriolabeitia, E.; Alegre-Requena, J. V.; Santamaria, J. A Highly-Active Chemodynamic Agent Based on In Situ Generated Copper Complexes from Copper Hexacyanoferrate Nanoparticles. *Small* **2025**, *21* (13), 2412355.
(63) Liu, Y.; Zhen, W.; Jin, L.; Zhang, S.; Sun, G.; Zhang, T.; Xu, X.; Song, S.; Wang, Y.; Liu, J.; Zhang, H. All-in-One Theranostic Nanoagent with Enhanced Reactive Oxygen Species Generation and Modulating Tumor Microenvironment Ability for Effective Tumor Eradication. *ACS Nano* **2018**, *12* (5), 4886−4893.
(64) Shi, L.; Newcomer, E.; Son, M.; Pothanamkandathil, V.; Gorski, C. A.; Galal, A.; Logan, B. E. Metal-Ion Depletion Impacts the Stability and Performance of Battery Electrode Deionization over Multiple Cycles. *Environ. Sci. Technol.* **2021**, *55* (8), 5412−5421.
(65) Xing, Z.; Ju, Z.; Yang, J.; Xu, H.; Qian, Y. One-step solid state reaction to selectively fabricate cubic and tetragonal CuFe2O4 anode material for high power lithium ion batteries. *Electrochim. Acta* **2013**, *102*, 51−57.
(66) Wessells, C. D.; Huggins, R. A.; Cui, Y. Copper hexacyanoferrate battery electrodes with long cycle life and high power. *Nat. Commun.* **2011**, *2* (1), 550.
(67) Bonet-Aleta, J.; Hueso, J. L.; Sanchez-Uriel, L.; Encinas-Gimenez, M.; Irusta, S.; Martin-Duque, P.; Martinez, G.; Santamaria, J. Synergistic assembly of gold and copper-iron oxide nanocatalysts to promote the simultaneous depletion of glucose and glutathione. *Mater. Tod. Chem.* **2023**, *29*, 101404.
(68) Boström, H. L. B.; Collings, I. E.; Daisenberger, D.; Ridley, C. J.; Funnell, N. P.; Cairns, A. B. Probing the Influence of Defects, Hydration, and Composition on Prussian Blue Analogues with Pressure. *J. Am. Chem. Soc.* **2021**, *143* (9), 3544−3554.
(69) Matsuda, T.; Kim, J.; Moritomo, Y. Control of the alkali cation alignment in Prussian blue framework. *Dalton Trans.* **2012**, *41* (25), 7620−7623.
(70) Wang, X.; Wang, W.-X. Cell-Type-Dependent Dissolution of CuO Nanoparticles and Efflux of Cu Ions following Cellular Internalization. *Environ. Sci. Technol.* **2022**, *56* (17), 12404−12415.
(71) Gratton, S. E. A.; Ropp, P. A.; Pohlhaus, P. D.; Luft, J. C.; Madden, V. J.; Napier, M. E.; DeSimone, J. M. The effect of particle design on cellular internalization pathways. *Proc. Natl. Acad. Sci. U.S.A.* **2008**, *105* (33), 11613−11618.
(72) Santo, C. E.; Lam, E. W.; Elowsky, C. G.; Quaranta, D.; Domaille, D. W.; Chang, C. J.; Grass, G. Bacterial killing by dry metallic copper surfaces. *Appl. Environ. Microbiol.* **2011**, *77* (3), 794−802.
(73) Quaranta, D.; Krans, T.; Santo, C. E.; Elowsky, C. G.; Domaille, D. W.; Chang, C. J.; Grass, G. Mechanisms of contact-mediated killing

https://doi.org/10.1021/cbmi.5c00237
Chem. Biomed. Imaging XXXX, XXX, XXX−XXX

of yeast cells on dry metallic copper surfaces. *Appl. Environ. Microbiol.* **2011**, *77* (2), 416−426.
(74) Grimm, J. B.; Muthusamy, A. K.; Liang, Y.; Brown, T. A.; Lemon, W. C.; Patel, R.; Lu, R.; Macklin, J. J.; Keller, P. J.; Ji, N.; Lavis, L. D. A general method to fine-tune fluorophores for live-cell and in vivo imaging. *Nat. Methods* **2017**, *14* (10), 987−994.
(75) Chen, L.; Min, J.; Wang, F. Copper homeostasis and cuproptosis in health and disease. *Signal Transduct. Target. Ther.* **2022**, *7* (1), 378.
(76) Ohgami, R. S.; Campagna, D. R.; McDonald, A.; Fleming, M. D. The Steap proteins are metalloreductases. *Blood* **2006**, *108* (4), 1388−1394.
(77) Wang, Z.; Li, N.; Zhao, J.; White, J. C.; Qu, P.; Xing, B. CuO Nanoparticle Interaction with Human Epithelial Cells: Cellular Uptake, Location, Export, and Genotoxicity. *Chem. Res. Toxicol.* **2012**, *25* (7), 1512−1521.
(78) Rennick, J. J.; Johnston, A. P. R.; Parton, R. G. Key principles and methods for studying the endocytosis of biological and nanoparticle therapeutics. *Nat. Nanotechnol.* **2021**, *16* (3), 266−276.
(79) Taki, M.; Iyoshi, S.; Ojida, A.; Hamachi, I.; Yamamoto, Y. Development of highly sensitive fluorescent probes for detection of intracellular copper(I) in living systems. *J. Am. Chem. Soc.* **2010**, *132* (17), 5938−5939.
(80) Gao, L.; Zhuang, J.; Nie, L.; Zhang, J.; Zhang, Y.; Gu, N.; Wang, T.; Feng, J.; Yang, D.; Perrett, S.; Yan, X. Intrinsic peroxidase-like activity of ferromagnetic nanoparticles. *Nat. Nanotechnol.* **2007**, *2* (9), 577−583.
(81) Chen, J.; Wang, Q.; Huang, L.; Zhang, H.; Rong, K.; Zhang, H.; Dong, S. Prussian blue with intrinsic heme-like structure as peroxidase mimic. *Nano Res.* **2018**, *11* (9), 4905−4913.
(82) Fu, J.; Shao, Y.; Wang, L.; Zhu, Y. Lysosome-controlled efficient ROS overproduction against cancer cells with a high pH-responsive catalytic nanosystem. *Nanoscale* **2015**, *7* (16), 7275−7283.
(83) Walsh, M. J.; Ahner, B. A. Determination of stability constants of Cu(I), Cd(II) & Zn(II) complexes with thiols using fluorescent probes. *J. Inorg. Biochem.* **2013**, *128*, 112−123.
(84) Drew, R.; Miners, J. O. The effects of buthionine sulphoximine (BSO) on glutathione depletion and xenobiotic biotransformation. *Biochem. Pharmacol.* **1984**, *33* (19), 2989−2994.
(85) Morgan, M. T.; Nguyen, L. A. H.; Hancock, H. L.; Fahrni, C. J. Glutathione limits aquacopper(I) to sub-femtomolar concentrations through cooperative assembly of a tetranuclear cluster. *J. Biol. Chem.* **2017**, *292* (52), 21558−21567.
(86) Hatori, Y.; Clasen, S.; Hasan, N. M.; Barry, A. N.; Lutsenko, S. Functional Partnership of the Copper Export Machinery and Glutathione Balance in Human Cells. *J. Biol. Chem.* **2012**, *287* (32), 26678−26687.
(87) Singh, A.; Venkannagari, S.; Oh, K. H.; Zhang, Y. Q.; Rohde, J. M.; Liu, L.; Nimmagadda, S.; Sudini, K.; Brimacombe, K. R.; Gajghate, S.; et al. Small Molecule Inhibitor of NRF2 Selectively Intervenes Therapeutic Resistance in KEAP1-Deficient NSCLC Tumors. *ACS Chem. Bio.* **2016**, *11* (11), 3214−3225.
(88) Davies, T. G.; Wixted, W. E.; Coyle, J. E.; Griffiths-Jones, C.; Hearn, K.; McMenamin, R.; Norton, D.; Rich, S. J.; Richardson, C.; Saxty, G.; et al. Monoacidic Inhibitors of the Kelch-like ECH-Associated Protein 1: Nuclear Factor Erythroid 2-Related Factor 2 (KEAP1:NRF2) Protein-Protein Interaction with High Cell Potency Identified by Fragment-Based Discovery. *J. Med. Chem.* **2016**, *59* (8), 3991−4006.
(89) MacLeod, A. K.; McMahon, M.; Plummer, S. M.; Higgins, L. G.; Penning, T. M.; Igarashi, K.; Hayes, J. D. Characterization of the cancer chemopreventive NRF2-dependent gene battery in human keratinocytes: demonstration that the KEAP1-NRF2 pathway, and not the BACH1-NRF2 pathway, controls cytoprotection against electrophiles as well as redox-cycling compounds. *Carcinogenesis* **2009**, *30* (9), 1571−1580.
(90) Cvetko, F.; Caldwell, S. T.; Higgins, M.; Suzuki, T.; Yamamoto, M.; Prag, H. A.; Hartley, R. C.; Dinkova-Kostova, A. T.; Murphy, M. P. Nrf2 is activated by disruption of mitochondrial thiol homeostasis but not by enhanced mitochondrial superoxide production. *J. Biol. Chem.* **2021**, *296*, 100169.
(91) Harvey, C. J.; Thimmulappa, R. K.; Singh, A.; Blake, D. J.; Ling, G.; Wakabayashi, N.; Fujii, J.; Myers, A.; Biswal, S. Nrf2-regulated glutathione recycling independent of biosynthesis is critical for cell survival during oxidative stress. *Free Radic Biol. Med.* **2009**, *46* (4), 443−453.
(92) Itoh, K.; Wakabayashi, N.; Katoh, Y.; Ishii, T.; Igarashi, K.; Engel, J. D.; Yamamoto, M. Keap1 represses nuclear activation of antioxidant responsive elements by Nrf2 through binding to the amino-terminal Neh2 domain. *Genes Dev.* **1999**, *13* (1), 76−86.
(93) Banci, L.; Bertini, I.; Ciofi-Baffoni, S.; Kozyreva, T.; Zovo, K.; Palumaa, P. Affinity gradients drive copper to cellular destinations. *Nature* **2010**, *465* (7298), 645−648.
(94) Polishchuk, E. V.; Concilli, M.; Iacobacci, S.; Chesi, G.; Pastore, N.; Piccolo, P.; Paladino, S.; Baldantoni, D.; van Ijzendoorn, S. C. D.; Chan, J.; et al. Wilson Disease Protein ATP7B Utilizes Lysosomal Exocytosis to Maintain Copper Homeostasis. *Dev. Cell* **2014**, *29* (6), 686−700.
(95) Cater, M. A.; La Fontaine, S.; Shield, K.; Deal, Y.; Mercer, J. F. B. ATP7B Mediates Vesicular Sequestration of Copper: Insight Into Biliary Copper Excretion. *Gastroenterology* **2006**, *130* (2), 493−506.
(96) Zhang, S.; Gao, H.; Bao, G. Physical Principles of Nanoparticle Cellular Endocytosis. *ACS Nano* **2015**, *9* (9), 8655−8671.
(97) Behzadi, S.; Serpooshan, V.; Tao, W.; Hamaly, M. A.; Alkawareek, M. Y.; Dreaden, E. C.; Brown, D.; Alkilany, A. M.; Farokhzad, O. C.; Mahmoudi, M. Cellular uptake of nanoparticles: journey inside the cell. *Chem. Soc. Rev.* **2017**, *46* (14), 4218−4244.
(98) Lim, C. M.; Cater, M. A.; Mercer, J. F. B.; La Fontaine, S. Copper-dependent interaction of glutaredoxin with the N termini of the copper-ATPases (ATP7A and ATP7B) defective in Menkes and Wilson diseases. *Biochem. Biophys. Res. Commun.* **2006**, *348* (2), 428−436.
(99) Kuo, Y. M.; Zhou, B.; Cosco, D.; Gitschier, J. The copper transporter CTR1 provides an essential function in mammalian embryonic development. *Proc. Natl. Acad. Sci. U. S. A.* **2001**, *98* (12), 6836−6841.
(100) Das, A.; Ash, D.; Fouda, A. Y.; Sudhahar, V.; Kim, Y.-M.; Hou, Y.; Hudson, F. Z.; Stansfield, B. K.; Caldwell, R. B.; McMenamin, M.; et al. Cysteine oxidation of copper transporter CTR1 drives VEGFR2 signalling and angiogenesis. *Nat. Cell Biol.* **2022**, *24* (1), 35−50.
(101) Lugano, R.; Ramachandran, M.; Dimberg, A. Tumor angiogenesis: causes, consequences, challenges and opportunities. *Cell. Mol. Life Sci.* **2020**, *77* (9), 1745−1770.

https://doi.org/10.1021/cbmi.5c00237
Chem. Biomed. Imaging XXXX, XXX, XXX−XXX